**SDHA gain-of-function engages inflammatory mitochondrial retrograde signaling via KEAP1–Nrf2**

Anne-Valérie Burgener[1, 22], Glenn R. Bantug[1, 21, 22], Benedikt Meyer[2], Rebecca Higgins[3], Adhideb Ghosh[3, 4], Olivier Bignucolo[5], Eric H. Ma[6, 7, 8], Jordan Löliger[1], Gunhild Unterstab[1], Marco Geigges[9], Rebekah Steiner[1], Michel Enamorado[10, 11], Robert Ivanek[12], Danielle Hunziker[1], Alexander Schmidt[13], Bojana Müller-Durovic[1], Jasmin Grählert[1], Raja Epple[1], Sarah Dimeloe[14], Jonas Lötscher[1], Ursula Sauder[15], Monika Ebnöther[16], Bettina Burger[3], Ingmar Heijnen[17], Sarai Martínez-Cano[10], Nathan Cantoni[18], Rolf Brücker[19], Christian R. Kahlert[20], David Sancho[10], Russell G. Jones[6, 7, 8], Alexander Navarini[3], Mike Recher[2, 22], Christoph Hess[1, 21, 22]

[1] Immunobiology Laboratory, Department of Biomedicine, University and University Hospital of Basel, Basel, Switzerland
[2] Immunodeficiency Laboratory, Department of Biomedicine, University and University Hospital of Basel, Basel, Switzerland
[3] Division of Dermatology and Dermatology Laboratory, Department of Biomedicine, University and University Hospital of Basel, Basel, Switzerland
[4] Competence Center for Personalized Medicine University of Zürich/ETH, Zürich, Switzerland
[5] Department of Pharmacology and Toxicology, University of Lausanne, Lausanne, Switzerland
[6] Center for Cancer and Cell Biology, Van Andel Institute, Grand Rapids, MI, 49503, USA
[7] Goodman Cancer Research Centre, McGill University, Montreal, QC, H3A 1A3, Canada
[8] Department of Physiology, McGill University, Montreal, QC, H3G 1Y6, Canada
[9] Epigenomics Group, D-BSSE, ETH Zürich, Basel, Switzerland
[10] Immunobiology Laboratory, Centro Nacional de Investigaciones Cardiovasculares Carlos III (CNIC), Madrid, Spain
[11] Mucosal Immunology Section, Laboratory of Parasitic Diseases, NIAID, NIH, Washington DC, USA
[12] Bioinformatics Facility, Department of Biomedicine, University and University Hospital of Basel, Basel, Switzerland
[13] Proteomics Core Facility, Biozentrum, University of Basel, Basel, Switzerland
[14] Institute of Immunology and Immunotherapy, University of Birmingham, Birmingham, UK
[15] Electron Microscopy Core Facility, Biozentrum, University of Basel, Basel, Switzerland
[16] Division of Hematology and Oncology, Claraspital, Basel, Switzerland
[17] Division Medical Immunology, Laboratory Medicine, University Hospital Basel, Basel, Switzerland
[18] Division of Hematology, Cantonal Hospital of Aarau, Aargau, Switzerland
[19] Division of Internal Medicine and Rheumatology, Hospital St. Anna, Luzern, Switzerland
[20] Division of Infectious Diseases, Children's Hospital of St. Gallen, St. Gallen, Switzerland
[21] Cambridge Institute of Therapeutic Immunology & Infectious Disease, Department of Medicine, University of Cambridge, UK

[22] Equal contribution

Correspondence to: Christoph Hess, MD PhD

Immunobiology Laboratory
Department of Biomedicine
University and University Hospital of Basel
20 Hebelstrasse
CH-4031 Basel
Switzerland
Phone: +41(0)61.265.44.75

and

Cambridge Institute of Therapeutic Immunology & Infectious Disease (CITIID)
Jeffrey Cheah Biomedical Centre
Cambridge Biomedical Campus
University of Cambridge
Puddicombe Way
Cambridge CB2 0AW
UK

Email: chess@uhbs.ch; ch818@cam.ac.uk

**ABSTRACT**

Whether screening the metabolic activity of immune cells facilitates discovery of molecular pathology remains unknown. Here we prospectively screened the extracellular acidification rate (ECAR) as a measure of glycolysis and the oxygen consumption rate (OCR) as a measure of mitochondrial respiration in B cells from patients with primary antibody deficiency (PAD). The highest OCR values were detected in three study participants with persistent polyclonal B cell lymphocytosis (PPBL). Exome sequencing identified germline mutations in *SDHA,* which encodes succinate dehydrogenase subunit A, in all three patients with PPBL. SDHA gain-of-function led to accumulation of fumarate in PPBL B cells, which engaged the KEAP1–Nrf2 system to drive the transcription of genes encoding inflammatory cytokines. In a single patient trial, blocking the activity of the cytokine IL-6 *in vivo* prevented systemic inflammation and ameliorated clinical disease. Overall, our study has identified pathological mitochondrial retrograde signaling as a disease modifier in PAD.

Primary immunodeficiency disorders (PIDs) are rare genetic syndromes arising from defects in the immune system[1]. The majority of PID patients display primary antibody deficiency (PAD) that can develop due to B cell intrinsic defects[2]. The causes and genetic background of PADs are complex and pathogenic mutations have been identified only in a minority of cases[3, 4, 5]. PADs present with a spectrum of clinical problems, ranging from infections to autoinflammation, autoimmunity, lymphoproliferation and enteropathy. Non-infectious complications are typically unaffected by immunoglobulin replacement therapy and contribute to excess mortality[6]. The spectrum of clinical presentation is broad even in patients harboring the same pathogenic mutations, pointing to disease modifiers shaping clinical features[6].

Cellular metabolism governs immune cell function[7, 8, 9]. Specifically, various facets of glycolysis and glutaminolysis impact the function of B cells[10, 11, 12, 13]. Glutaminolysis can contribute to ATP production, and glutamine-derived α-ketoglutarate (α-KG) serves as an anaplerotic source of tricarboxylic acid (TCA) cycle metabolites[14]. Mitochondrial oxidative phosphorylation (OxPhos) produces most of the ATP required for anabolic processes in immune cells[15]. Non-bioenergetic features of mitochondria also regulate immune cell function. Production of mitochondrial reactive oxygen species (mROS) has been linked to the activation of the transcription factor NFAT in $CD4^+$ T cells and to inhibition of the B cell antigen receptor (BCR) signaling in B cells[16, 17]. In T cells, mitochondrial function and epigenetic remodeling are interlinked via pyruvate oxidation and conversion of pyruvate-derived citrate to acetyl-CoA, which is required for histone acetylation[18, 19]. Metabolites of the TCA cycle can also directly activate (α-KG), or inhibit (fumarate, succinate) dioxygenases involved in histone and DNA demethylation, thus modulating transcriptional activity. This process of mitochondrial metabolites impacting nuclear transcriptional processes is known as 'mitochondrial retrograde signaling'[20]. Indeed, the α-KG/fumarate+succinate ratio dictates epigenetic changes and transcriptional programs in macrophages[21, 22]. Protein succination, the fumarate-dependent, non-enzymatic addition of a succinyl group to thiol groups in proteins, provides another emerging link between mitochondrial function and transcriptional activity of cells[23].

In this study we assessed whether B cell metabolic screening can identify PAD patients suffering from disease modifying metabolic dysregulation. We found that B cell OxPhos served as a functional biomarker that helped decipher a pathogenic immunometabolic dysregulation in B cells, which directed a successful clinical intervention.

## RESULTS

### Oxygen consumption rates are increased in PPBL B cells

To establish normal values for mitochondrial respiration and glycolysis in B cells, we measured oxygen consumption rates (OCR) and extracellular acidification rates (ECAR), respectively, from 15 healthy individuals and 14 patients with PAD using a metabolic flux analyzer. We detected higher OCR in PAD B cells compared to healthy controls (HC), while ECAR was similar in both groups (**Fig. 1a**). No strong age dependence or differences between sex or CMV sero-positivity in OCR or ECAR was observed in either group (Supplementary **Fig. 1a,b**). Basal OCR from 3 PAD patients (patients 1, 8 and 9), all diagnosed with persistent polyclonal B cell lymphocytosis (PPBL), was 2.2-fold higher than in HC (Supplementary **Table 1a**). PPBL is a rare immune dysregulation characterized by expansion of $IgD^+CD27^+$ marginal zone-like (MZ-like) B cells, elevated IgM, and low IgG in the serum[24, 25]. Patient 1, 8 and 9, the only PPBL patients initially included in this study, all had clinically manifest disease (Supplementary **Table 1a, b**). Patient 9 had the most severe disease course, characterized by systemic inflammation, cutaneous small-vessel vasculitis (leukocytoclastic vasculitis), and periaortitis (**Fig. 1b**). About 80% of total B cells from patients 1, 8 and 9 were $IgD^+CD27^+TACI^+CD24^+CD38^-$ cells, reminiscent of murine marginal zone B cells (hereafter marginal zone (MZ)-like B cells), compared to approx. 20% in HC (**Fig. 1c** and Supplementary **Fig. 1c**). Thus, for downstream experiments, we used total B cells from PPBL patients, which are primarily MZ-like B cells (hereafter PPBL B cells). Proliferation of PPBL B cells was similar to that of $IgD^+CD27^-$ naïve B cells and $IgD^+CD27^+$ MZ-like B cells from HC, following stimulation with CpG or IL-21+CD40L (Supplementary **Fig. 1d**). Further, OCR and ECAR of HC MZ-like B cells was similar to that of total B cells from HC, but less than OCR from PPBL B cells (**Fig. 1d**), indicating that hyper-respiration was PPBL B cell-intrinsic. Both OCR and ECAR of total B cells from all 3 PPBL patients remained stable ~12 months after baseline measurements (**Fig. 1d**). The high OCR in B cells from patient 9 was not affected by treatment with the rapamycin synthetic analogue sirolimus (**Fig. 1e**). ECAR was similarly increased in PPBL B cells and HC total B cells treated with IL-21+CD40L (**Fig. 1f**), and glucose uptake under activating conditions was also similar (**Fig. 1g**), indicating glycolysis was not dysregulated in PPBL B cells. The relative distribution of $CD27^+CD45RO^-$ naïve, $CD27^+CD45RO^+$ central memory ($T_{CM}$), and $CD27^-CD45RO^+$ effector memory ($T_{EM}$) $CD4^+$ and $CD8^+$ T cells and the proliferation of total $CD4^+$ and $CD8^+$ T cells stimulated with antibodies against CD3+CD28 were similar between HC and PPBL patients (Supplementary **Fig. 1e**,**f**). Additionally, production of IFN-γ in CMV-specific T cells, basal respiration, glycolysis and the mitochondrial membrane potential were similar between the two groups (Supplementary **Fig. 1g,h**). As such, total B cells from 3 PPBL patients had increased OCR compared to HC MZ-like B cells, while there was no evidence for altered T cell function or metabolism.

**Complex II is hyper-functional in PPBL B cells**

Next, we analyzed mitochondria in PPBL B cells by electron microscopy. Mitochondria cristae, matrix morphology, number and area per cell, mitochondrial shape, as well as total cell area were similar between PPBL B cells and HC total B cells (Supplementary **Fig. 2a**). The protein abundance of NDUFB8 (complex I), succinate dehydrogenase (SDH) B (complex II), UQCRC2 (complex III), COX II (complex IV) and ATP5A (complex V) were also similar between HC and PPBL total B cells (Supplementary **Fig. 2b**). Using blue native (BN)-PAGE immunoblot analyses on mitochondria enriched fractions, expression of complexes I–IV, formation of complex I containing super-complexes (I+III and I+III+IV) and assembly of complex III+IV was similar between EBV-immortalized B cell lines (hereafter B-LCLs) derived from HC MZ-like B cells and PPBL B cells (Supplementary **Fig. 2c**). Mitochondrial membrane potential, as measured using MTR and MTDR, was moderately increased in PPBL B cells compared to HC MZ-like B cells (Supplementary **Fig. 2d**).

The enzymatic activities of complexes I, IV and V were identical, while the activity of complex II was robustly increased in all 3 PPBL B-LCLSs derived from each patient compared to HC MZ-like B-LCLs (**Fig. 2a**), indicating a complex II-intrinsic gain-of-function in these cells. To test the function of respiratory complexes I–IV in their normal structural context, their contribution to oxygen consumption was assessed in permeabilized cells[26]. A selective increase in complex II function, which was not altered by the complex I inhibitor rotenone, was observed in PPBL B-LCLs compared to HC MZ-like B-LCLs (**Fig. 2b,c**). Immunoblot analyses of the complex I subunit Grim19, involved in electron transfer, and SDHA, the major catalytic subunit of complex II, did not detect differences in protein abundance between patient B-LCLs and HC MZ-like B-LCLs (**Fig. 2d**). These findings revealed a subtle, yet robust, difference in mitochondrial function that was linked to increased SDH-complex II activity in PPBL B-LCLs compared to HC MZ-like B-LCLs.

**Glutaminolysis contributes to TCA fueling in PPBL B cells**

To gain insight into the metabolic landscape of B cells from PPBL patients, we performed metabolomic analyses on total PPBL B cells and sorted $IgD^{+}CD27^{+}$ MZ-like B cells from HC. Several glycolytic intermediates such as dihydroxyacetone phosphate (DHAP), 2-phosphoglycerate (2-PG) and phosphoenolpyruvate (PEP) were increased in PPBL B cells compared to HC MZ-like B cells, whereas pyruvate was similarly abundant (**Fig. 3a**). Moreover, we detected an almost 6-fold increase in fumarate and malate in PPBL B cells compared to HC MZ-like B cells (**Fig. 3a**). Other TCA cycle metabolites (citrate, aconitate and $\alpha$-KG), as well as glutamate were also more abundant in PPBL B cells than in HC MZ-like B cells (**Fig. 3a**). These findings suggested increased glutaminolysis in PPBL B cells compared to HC MZ-like B cells. As observed in primary PPBL B cells, accumulation of fumarate was also evident in PPBL

derived B-LCLs (**Fig. 3b**). Of note, whereas the fumarate/succinate ratio was increased in PPBL B cells, the α-KG/fumarate+succinate ratio was similar between HC MZ-like and PPBL B cells (**Fig. 3c**), because α-KG was also more abundant in PPBL B cells. Using metabolic tracing studies, abundant m+5 (α-KG) and m+4 (succinate, fumarate, malate and citrate) isotopologues of TCA cycle metabolites were detected in primary PPBL B cells cultured with $^{13}$C-glutamine, whilst M+2 and M+4 isotopologues derived from $^{13}$C-glucose were less abundant (**Fig. 3d**), indicating that glutaminolysis contributed to anaplerotic fueling of the TCA cycle in PPBL B cells. These results revealed the accumulation of fumarate in PPBL B cells compared to HC MZ-like B cells, and indicated that glutamine is an important fuel source of the TCA cycle in PPBL B cells.

**PPBL B cells have an inflammatory transcriptional profile**

We then investigated the transcriptional profile of primary PPBL B cells. Of the 13'107 gene transcripts that were detected, mRNA abundance of 1'878 genes (14.33%) differed in a statistically significant manner between PPBL B cells and HC MZ-like B cells, as indicated by unsupervised hierarchical clustering of the samples (**Fig. 4a**). Genes typically expressed in MZ-like B cells, such as ITM2C, JAM3 and CD80 were also abundant in PPBL B cells[27, 28](**Fig. 4b**), suggesting their close relationship. Metabolic genes, specifically those involved in the TCA cycle (PC, IDH), glycolysis (HK, ALDOC) and glutamine metabolism (DDAH2) were differentially expressed between primary PPBL B cells and HC MZ-like B cells, but fold expression differences were mostly moderate and ranged between -2 and 2 $\log_2$-fold (Supplementary **Fig. 3a**). Of note, the transcripts of complex II genes were not differentially expressed (**Fig. 4c**). Genes encoding other respiratory complexes were different in PPBL B cells and HC MZ-like B cells, but the fold expression differences typically ranged between -1 and 1 $\log_2$-fold (Supplementary **Fig. 3b**). On the other hand, transcripts annotated to the inflammatory response and the IL-6–Jak–STAT3 pathway were enriched in PPBL B cells relative to HC MZ-like B cells (**Fig. 4d**). Transcripts for *CXCL8, IL1B*, *CCL5*, *IL6* and *TNF*, all induced during inflammation, were consistently more abundant in PPBL B cells than HC MZ-like B cells (**Fig. 4e**). Moreover, the abundance of IL-6 and IL-8 protein was also increased in the supernatant of PPBL B-LCLs compared to HC MZ-like B-LCLs (**Fig. 4f**). In 2 separate measurements, the concentration of IL-6 was moderately increased in the serum of patient 8 relative to mean clinical values in HC (**Fig. 4g**). Together, these findings demonstrated that PPBL B cells shared similar transcriptomic profiles as MZ-like B cells, however, these cells also displayed increased inflammatory gene expression.

**SDH drives an inflammatory phenotype in PPBL B cells**

To assess whether hyperactive SDH and increased cytokine production in PPBL B cells were linked, we probed the effect of the SDH inhibitor 3-nitropropionic acid (3-NPA) on mitochondrial respiration and

IL-6 production. Basal OCR, complex II respiration and IL-6 production under basal conditions and following IL-21+CD40L stimulation were reduced in PPBL B-LCLs treated with 3-NPA compared to untreated controls (**Fig. 5a**). Targeting *SDHA* expression with siRNA in PPBL B-LCLs reduced SDHA protein expression by 40%, complex II respiration by 25%, and it also diminished the production of IL-6 (**Fig. 5b**), indicating that SDHA activity in PPBL B cells was associated with increased IL-6 production. Monomethyl fumarate (a cell-permeable form of fumarate) also enhanced IL-6 production by 1.6-fold in treated cells compared to untreated controls (Supplementary **Fig. 4a**). Monomethyl fumarate is more electrophilic than fumarate, thus introducing the potential for unwanted reactivity. To induce a buildup of endogenous fumarate, we depleted fumarate hydratase (*FH*) in HC MZ-like B-LCLs using siRNA, which resulted in increased abundance of intracellular fumarate and production of IL-6 compared to si-control treated cells (**Fig. 5c**), indicating excess fumarate was sufficient to boost IL-6 production. Modulation of pyruvate import, or inhibition of glutaminolysis, did not have a major impact on IL-6 production in PPBL B-LCLs (Supplementary **Fig. 4b**), pointing to the metabolic flexibility of these cells in fueling SDH activity. Next, we performed whole exome sequencing (WES) of primary PPBL B cells from blood. Initial interrogation of WES data did not identify known genetic abnormalities previously linked to PIDs (data not shown). Focusing on rare genetic variants in genes encoding mitochondrial proteins revealed rare variants (G135G, A45T, A449V) with high Combined Annotation Dependent Depletion (CADD) scores in the *SDHA* gene from all three PPBL patients (Supplementary **Table 2**). To independently confirm these genetic findings, an additional patient with clinical PPBL (patient 15; Supplementary **Table 1a**) was recruited into the study. Total B cells from patient 15 also displayed elevated OCR but not ECAR compared to total B cells from HC (Supplementary **Fig. 4c**). WES identified an L649E frame shift variant in the *SDHA* gene of patient 15 (Supplementary **Table 2**). Next, we introduced the A45T mutation from patient 8 into one allele of SDHA in HC MZ-like B-LCLs using CRISPR/Cas9 technology. Expression of the SDHA-A45T mutant increased complex II-specific OCR and IL-6 production compared to (what) cells transfected with control oligonucleotides (**Fig. 5d**), suggesting that gain-of-function mutations in SDHA promoted an inflammatory response.

SDHA catalyzes oxidation of succinate to fumarate and transfers the resulting electrons to SDHB via the electron transporting coenzyme flavin adenine dinucleotide (FAD). Because the Ala45 residue is located at the highly flexible N-terminal segment of SDHA, which interacts with SDHB, the highly hydrophilic side-chain of Thr in the A45T variant could form hydrogen bonds with SDHB, which stabilizes the complex and favors complex II respiration. Using molecular dynamics (MD) simulation, H-bonds between the N-terminal segment of SDHA and residues Asp20-Pro21-Asp22 of SDHB formed randomly and at the same rate in both wild-type SDHA (WT-SDHA) and SDHA-A45T (Supplementary **Fig. 4d** and Supplementary **Video 1**). However, while interactions between SDHA and SDHB lasted 2-3 ns and

involved mostly one atom pair in WT-SDHA, these interactions lasted 10-12 ns and involved 2-3 atom-pairs in SDHA-A45T (**Fig. 5e,** Supplementary **Fig. 4d** and Supplementary Video **V1**), indicating a stronger hydrogen bond interaction between SDHA-A45T and SDHB. Asp20 and Asp22 of SDHB accounted for more than 90% of the hydrogen bonds with Ala43, Ser44 and Lys46 of SDHA, whilst hydrogen bonds with either Ala45 or the mutant variant Thr45 were similarly negligible (Supplementary **Fig. 4e**). However, Thr45 in SDHA-A45T formed stronger intra-molecular interactions with Arg458, Phe459, Asp511, Arg512 and Met514 residues on SDHA compared to Ala45 in WT-SDHA (Supplementary **Fig. 4f**). These new intra-molecular interactions maintained the SDHA N-terminal segment in a particular conformation that favored interaction with SDHB. Aligning with the MD data, compound SDHA-SDHB activity, measured spectrophotometrically, was higher in B-LCLs from patient 8 as compared to HC MZ-like B-LCLs (Supplementary **Fig. 4g**). These results suggested that increased interaction between SDHA-A45T and SDHB may drive the increased function of mutant SDH.

**Fumarate drives Nrf2-dependent transcription of IL-6**

In human monocytes, fumarate accumulation during initial stimulation augments the production of inflammatory cytokines upon re-activation by inhibiting histone demethylation (known as 'trained immunity')[21]. Transcriptomic analysis of total PPBL B cells and 'fumarate-trained' monocytes[21] indicated the gene expression profiles of these cell types did not correlate (Supplementary **Fig. 5a**). Additionally, no difference in pan-histone 3 (H3) methylation was detected in total B cells from PPBL patients and HC (Supplementary **Fig. 5b**), ruling out global effects on histone methylation. Succination of proteins by fumarate can alter function[29, 30]. Using an antibody that recognized the stable adduct formed by succination, i.e. S-2-(succino)cysteine (2SC), for immunoblot analysis indicated that protein succination was more pronounced in primary PPBL B cells compared to HC total B cells, with the most prominent band appearing at a size between 60-70 kD (**Fig. 6a**). Succination of reactive cysteines on KEAP1 by fumarate has been described in cancer cells with loss-of-function mutations in FH and consequent accumulation of fumarate[31]. Re-probing stripped 2SC immunoblots with a monoclonal antibody against KEAP1 revealed a band at the same position as the prominent 2SC band in PPBL B cells (**Fig. 6a**). Succination was detected on KEAP1 immunoprecipitated from PPBL B-LCLs, but not on KEAP1 from HC MZ-like B-LCLs (**Fig. 6b**).

Constitutive binding of KEAP1 to the transcription factor Nrf2 targets Nrf2 for ubiquitin-dependent degradation[32, 33]. KEAP1 succination destabilizes KEAP1-Nrf2 interaction, allowing nuclear translocation of Nrf2 and the transcription of target genes[31, 34] and p62-mediated targeting of KEAP1 for autophagosomal degradation[35]. Using imaging flow cytometry, KEAP1 was found to be homogenously and diffusedly distributed in HC total B cells, whereas KEAP1 was sequestered to an undefined

cytoplasmic compartment in primary PPBL B cells (**Fig. 6c**). K67 is a KEAP1 activator that prevents KEAP1 degradation by blocking KEAP1 and phosphorylated-p62 interaction. Immunoblots indicated that the phosphorylation status of p62 was similar between PPBL B-LCLs and HC MZ-like B-LCLs under basal conditions as well as after IL-21+CD40L activation (**Fig. 6d**), indicating that K67 was able to prevent KEAP1 degradation in both B-LCL populations. K67 treatment of PPBL B-LCLs reduced IL-6 production compared to untreated controls (**Fig. 6d**). Additionally, primary PPBL B cells treated with K67 had lower Nrf2 nuclear accumulation compared to untreated HC (Supplementary **Fig. 5c**), demonstrating that stabilizing KEAP1 with K67 restricted Nrf2 activity. Of note, Nrf2 was more abundant in nuclei extracted from PPBL B-LCLs compared to HC MZ-like B-LCLs (**Fig. 6e**). Using GSEA, canonical targets of Nrf2, such as *GCLC* and *NQO1*, were not enriched in PPBL B cells compared to MZ-like B cells from HC (data not shown). However, quantification of transcripts by qPCR indicated a slightly higher abundance of GCLC, GLCM, NQO1 and TXNRD1 in PPBL B-LCLs compared to HC MZ-like B-LCLs (Supplementary **Fig. 5d**). Metabolomics analyses also identified increased abundance of glutathione (reduced GSH and oxidize GSSG) in primary PPBL B cells compared to MZ-like B cells from HC (Supplementary **Fig. 5d**). Further, the GSH/GSSG ratio in PPBL B cells was greater than in HC MZ-like B cells (data not shown), indicating a reductive state in PPBL B cells that is typically associated with constitutively active Nrf2[36].

Treatment with the Nrf2 inhibitor ML-385 reduced IL-6 production in non-activated and IL-21+CD40L-activated PPBL B-LCLs compared to untreated controls (**Fig. 6f**). ML-385 also largely abrogated monomethyl fumarate-driven production of IL-6 in MZ-like B-LCLs from HC (Supplementary **Fig. 5e**). Inversely, addition of the Nrf2 activator CDDO enhanced *NQO1* and *IL6* transcript abundance in PPBL and HC MZ-like B-LCLs under basal and IL-21+CD40L activating conditions (Supplementary **Fig. 5f**). Depletion of Nrf2 protein using siRNA interference robustly decreased the production of IL-6 mRNA and protein, in PPBL B-LCLs from all three patients compared to si-control transfected cells (**Fig. 6g**). Computational approaches identified Nrf2 binding motifs in the promoters of *IL6*, *IL1B* and *CXCL8* (Supplementary **Table 3**). ChIP-PCR indicated increased binding of Nrf2 binding in both predicted binding sites in the *IL6* promoter as well as to the promoter of the canonical Nrf2 targets NQO1 and HMOX1 in primary PPBL B cells compared to total B cells from HC (**Fig. 6h**). Lastly, inhibition of Nrf2 with ML385 in primary human B cells stimulated with CpG for 24 h blunted IL-6 production in $IgD^{+}CD27^{-}$ naïve B cells, and only had a moderate effect in $CD27^{+}$ memory B cells (Supplementary **Fig. 5g**), whereas treatment with ML385 had no appreciable effect on the surface expression of CD69, CD86, HLADR and CD71 in both subsets (Supplementary **Fig. 5g**). Activation of KEAP1 with K67 did not impact production of IL-6 in both B cell subsets (Supplementary **Fig. 5g**). Together, these data indicated that excess production of IL-6 in PPBL B cells was mediated by triggering the KEAP1–Nrf2 axis.

To test whether blocking IL-6 may have clinical efficacy, we treated patient 8 with a single dose of the IL-6 receptor-blocking antibody, tocilizumab. Four weeks after tocilizumab treatment, there was no detectable effect on antibody amounts, T and B cell numbers and B cell subset distribution in blood compared to pre-treatment blood samples (Supplementary **Table 4**), however, a slight reduction in CRP and BSR was observed (**Fig. 6i,** Supplementary **Fig. 5h**), suggesting reduced systemic inflammation. In addition, a clinical questionnaire taken before and two weeks into tocilizumab treatment suggested a beneficial impact of blocking IL-6 signaling in this patient with regard to symptoms of malaise and night sweats (**Fig. 6i,** Supplementary **Fig. 5h**). Together, mutations in *SDHA* drove accumulation of fumarate, which in turn led to inhibition of KEAP1, likely through succination, and the consequent Nrf2-driven inflammatory reprogramming of PPBL B cells (Supplementary **Fig. 5i**).

## DISCUSSION

In a prospective screening approach, we found that mitochondrial respiration was higher in B cells from patients with PAD. In a subset of patients with the most pronounced phenotype, hyper-respiration was determined to be due to gain-of-function variants in SDH, which were identified as the cause of fumarate accumulation, protein succination and inflammatory reprogramming of B cells in 3 PPBL patients. This inflammatory B cell reprogramming aligned with the clinical phenotype observed in these patients. In one PPBL patient, enhanced activity of SDH and accumulation of fumarate was traced to a gain-of-function mutation in *SDHA* (*SDHA*$^{A45T}$), and resulted in the increased production of IL-6.

Nrf2 activation following oxidative or electrophilic stress typically promotes an anti-inflammatory state by reducing intracellular ROS and by inhibiting the expression of pro-inflammatory cytokines and chemokines[37]. However, Nrf2 also supports inflammation by stabilizing the activation of NLRP3 and AIM2 inflammasomes, and by promoting inflammation in dextran sulfate sodium (DSS) colitis models and inducing IL-8 expression in kidney mesangial cells[38, 39]. These disparate roles in modulating inflammation suggest that Nrf2 function is context dependent, as evidenced by the protective and tumor promoting roles of Nrf2 in cancer[40]. In PPBL B cells, SDH-dependent accumulation of fumarate and succination of KEAP1 resulted in constitutive activation of Nrf2 that drove IL-6 expression. This agrees with reports that IL-6 transcription was mediated by Nrf2 in hepatocytes[41]. Systemic, low-grade inflammation observed in PPBL is potentially due to chronic elevated IL-6. Indeed, blockade of IL-6 signaling using tocilizumab in one PPBL patient alleviated inflammation and improved quality of life.

In PPBL, the majority of circulating B cells typically have an IgD$^{+}$CD27$^{+}$ MZ-like phenotype. MZ-like B cells produce inflammatory cytokines, reflecting their function as innate-like sensors of the immune response[27]. The genetic basis for this differentiation bias towards MZ-like B cells in PPBL remains unknown. Normal MZ-like B cell differentiation is dependent on Notch signaling in humans and mice[42, 43, 44, 45]. Notch1 expression in hepatocytes is partially mediated by Nrf2[46]. Increased basal Nrf2 activity could thus potentially enhance Notch signaling in transitional B cells and drive differentiation towards MZ-like B cells. Smoking is highly associated with progression to PPBL. Increased amounts of fumarate were reported in the serum of smokers[47]. Cigarette smoke can also enhance the expression of OxPhos proteins, including SDHA, in lung cells[48] and drive Nrf2 activation[49]. It can be speculated that activation of the fumarate–KEAP1–Nrf2 axis in cigarette smoking PPBL patients reflects an extreme variant of a much more common, smoking-associated immunometabolic dysregulation.

All four patients with PPBL carried different rare germline mutations in *SDHA*. We provided direct experimental evidence and detailed structural modeling to establish the effects of SDH-A45T (from patient 8) on SDHA function. *In silico*, Thr45 in SDHA-A45T stabilized the interactions between SDHA and SDHB. How the mutations in SDHA in patient 9 and patient 15 induced gain-of-function at the molecular

level remains to be determined. The mutation in patient 1 is synonymous. Synonymous rare codon variants play important functional roles in the regulation of co-translational folding and covalent modifications *in vivo*[50], the mutation identified here might be subject to a similar mechanism.

In summary, this study identified SDHA gain-of-function as a disease modifier in PPBL, driving fumarate accumulation, succination and inflammatory reprogramming of B cells. Representing the first example of a primary mitochondrial retrograde signaling pathology, our data point to therapeutic repurposing-strategies by uncovering druggable targets, namely SDHA, Nrf2 and IL-6 along this dysregulated molecular axis.

**ACKNOWLEDGEMENTS**

The authors would like to thank the patients that participated in the study; the flow sorting team and the microscopy core facility of the Department of Biomedicine, University and University Hospital of Basel; the Blood Donor Center affiliated with the University Hospital of Basel, as well as G. Hoenger, U.Duthaler, C. Gasser, J. Hirsiger, C. Berger, T. Daikeler, F. Marquardsen and F. Baldin for technical support and/or help with the clinical management of patients. Funding: C.H. and M.R. Gebert Rüf Foundation GRS-058/14; C.H. SNSF 31003A_172848; M.R. SNSF PP00P3_181038. This work was further supported by a grant from the Swiss National Supercomputing Centre (project ID SM09).

**AUTHOR CONTRIBUTIONS**

AVB performed and analyzed most experiments and helped writing the report; GRB performed experiments, conceived, coordinated and supervised the revision experiments and helped writing the report; RH and AG performed and analyzed the WES studies, AN analyzed and interpreted the WES studies and helped writing the report; OB performed the molecular dynamics studies and helped writing the report; EHM and RGJ performed, analyzed and interpreted metabolic tracing studies and helped writing the report; BB, BM, BMD, DH, GH, JG, JLöl, JLöt, RE, RS, SD and US planned, performed and interpreted various experiments. MEn, SMC and DS assessed mitochondrial super-complex formation. MG and RI performed bioinformatics analyses. AS planned, performed and analyzed proteomic experiments and helped writing the report. IH helped identifying PAD patients and performed immunologic analyses. CRK, MEb, NC and RB helped with recruiting PAD patients and coordinated clinical characterization and analyses. MR organized and supervised the PAD patient cohort, contributed to conceiving the study, supervised and advised experiments, analyzed and interpreted data, and helped writing the report. CH conceived the study, supervised and coordinated the research and wrote the report.

**COMPETING INTERESTS STATEMENT**

We declare that none of the authors have competing financial or non-financial interests as defined by Nature Research.

**REFERENCES (for main text only)**


1. Picard, C. et al. International Union of Immunological Societies: 2017 Primary Immunodeficiency Diseases Committee Report on Inborn Errors of Immunity. Journal of Clinical Immunology 38, 96-128 (2018).
2. Durandy, A., Kracker, S. & Fischer, A. Primary antibody deficiencies. Nature reviews. Immunology 13, 519-533 (2013).
3. Minegishi, Y. et al. An essential role for BLNK in human B cell development. Science 286, 1954-1957 (1999).
4. Silva, P. et al. Autosomal recessive agammaglobulinemia due to defect in mu heavy chain caused by a novel mutation in the IGHM gene. Genes Immun 18, 197-199 (2017).
5. van Zelm, M.C. et al. Human CD19 and CD40L deficiencies impair antibody selection and differentially affect somatic hypermutation. J Allergy Clin Immunol 134, 135-144 (2014).
6. Fischer, A. et al. Autoimmune and inflammatory manifestations occur frequently in patients with primary immunodeficiencies. The Journal of allergy and clinical immunology 140, 1388-1393.e1388 (2017).
7. Bantug, G.R., Galluzzi, L., Kroemer, G. & Hess, C. The spectrum of T cell metabolism in health and disease. Nature reviews. Immunology 18, 19-34 (2018).
8. Dimeloe, S., Burgener, A.-V., Grählert, J. & Hess, C. T-cell metabolism governing activation, proliferation and differentiation; a modular view. Immunology (2016).
9. Hess, C. & Kemper, C. Complement-Mediated Regulation of Metabolism and Basic Cellular Processes. Immunity 45, 240-254 (2016).
10. Boothby, M. & Rickert, R.C. Metabolic Regulation of the Immune Humoral Response. Immunity 46, 743-755 (2017).
11. Carr, E.L. et al. Glutamine uptake and metabolism are coordinately regulated by ERK/MAPK during T lymphocyte activation. Journal of immunology (Baltimore, Md. : 1950) 185, 1037-1044 (2010).
12. Jellusova, J. et al. Gsk3 is a metabolic checkpoint regulator in B cells. Nature immunology 18, 303-312 (2017).
13. Jiang, S., Yan, W., Wang, S.E. & Baltimore, D. Let-7 Suppresses B Cell Activation through Restricting the Availability of Necessary Nutrients. Cell metabolism 27, 393-403.e394 (2018).
14. Mehta, M.M., Weinberg, S.E. & Chandel, N.S. Mitochondrial control of immunity: beyond ATP. Nature reviews. Immunology 17, 608-620 (2017).
15. Tan, H. et al. Integrative Proteomics and Phosphoproteomics Profiling Reveals Dynamic

Signaling Networks and Bioenergetics Pathways Underlying T Cell Activation. Immunity 46, 488-503 (2017).
16. Ogura, M. et al. Mitochondrial reactive oxygen species suppress humoral immune response through reduction of CD19 expression in B cells in mice. European journal of immunology 47, 406-418 (2017).
17. Sena, L.A. et al. Mitochondria are required for antigen-specific T cell activation through reactive oxygen species signaling. Immunity 38, 225-236 (2013).
18. Bantug, G.R. et al. Mitochondria-Endoplasmic Reticulum Contact Sites Function as Immunometabolic Hubs that Orchestrate the Rapid Recall Response of Memory CD8+T Cells. Immunity (2018).
19. Gubser, P.M. et al. Rapid effector function of memory CD8+ T cells requires an immediate-early glycolytic switch. Nature immunology 14, 1064-1072 (2013).
20. Xiao, M. et al. Inhibition of α-KG-dependent histone and DNA demethylases by fumarate and succinate that are accumulated in mutations of FH and SDH tumor suppressors. Genes & development 26, 1326-1338 (2012).
21. Arts, R.J.W. et al. Glutaminolysis and Fumarate Accumulation Integrate Immunometabolic and Epigenetic Programs in Trained Immunity. Cell metabolism 24, 807-819 (2016).
22. Liu, P.-S. et al. α-ketoglutarate orchestrates macrophage activation through metabolic and epigenetic reprogramming. Nature immunology 18, 985-994 (2017).
23. Alderson, N.L. et al. S-(2-Succinyl)cysteine: a novel chemical modification of tissue proteins by a Krebs cycle intermediate. Archives of biochemistry and biophysics 450, 1-8 (2006).
24. Carulli, G. et al. Modifications in B-Lymphocyte Number and Phenotype in the Course of Pregnancy in a Woman with Persistent Polyclonal B-Cell Lymphocytosis: A Flow Cytometric Study. Journal of clinical and experimental hematopathology : JCEH 55, 77-82 (2015).
25. Salcedo, I., Campos-Caro, A., Sampalo, A., Reales, E. & Brieva, J.A. Persistent polyclonal B lymphocytosis: an expansion of cells showing IgVH gene mutations and phenotypic features of normal lymphocytes from the CD27+ marginal zone B-cell compartment. British journal of haematology 116, 662-666 (2002).
26. Salabei, J.K., Gibb, A.A. & Hill, B.G. Comprehensive measurement of respiratory activity in permeabilized cells using extracellular flux analysis. Nature protocols 9, 421-438 (2014).
27. Cerutti, A., Cols, M. & Puga, I. Marginal zone B cells: virtues of innate-like antibody-producing lymphocytes. Nature reviews. Immunology 13, 118-132 (2013).
28. Seifert, M. et al. Functional capacities of human IgM memory B cells in early inflammatory responses and secondary germinal center reactions. Proceedings of the National Academy of

Sciences of the United States of America 112, E546-555 (2015).
29. Blatnik, M., Thorpe, S.R. & Baynes, J.W. Succination of proteins by fumarate: mechanism of inactivation of glyceraldehyde-3-phosphate dehydrogenase in diabetes. Annals of the New York Academy of Sciences 1126, 272-275 (2008).
30. Kornberg, M.D. et al. Dimethyl fumarate targets GAPDH and aerobic glycolysis to modulate immunity. Science 17, eaan4665 (2018).
31. Adam, J. et al. Renal cyst formation in Fh1-deficient mice is independent of the Hif/Phd pathway: roles for fumarate in KEAP1 succination and Nrf2 signaling. Cancer cell 20, 524-537 (2011).
32. Itoh, K. et al. Keap1 represses nuclear activation of antioxidant responsive elements by Nrf2 through binding to the amino-terminal Neh2 domain. Genes Dev 13, 76-86 (1999).
33. Kobayashi, A. et al. Oxidative and electrophilic stresses activate Nrf2 through inhibition of ubiquitination activity of Keap1. Mol Cell Biol 26, 221-229 (2006).
34. Kinch, L., Grishin, N.V. & Brugarolas, J. Succination of Keap1 and activation of Nrf2-dependent antioxidant pathways in FH-deficient papillary renal cell carcinoma type 2. Cancer cell 20, 418-420 (2011).
35. Taguchi, K. et al. Keap1 degradation by autophagy for the maintenance of redox homeostasis. Proc Natl Acad Sci U S A 109, 13561-13566 (2012).
36. Shanmugam, G., Narasimhan, M., Tamowski, S., Darley-Usmar, V. & Rajasekaran, N.S. Constitutive activation of Nrf2 induces a stable reductive state in the mouse myocardium. Redox Biol 12, 937-945 (2017).
37. Ma, Q. Role of nrf2 in oxidative stress and toxicity. Annu Rev Pharmacol Toxicol 53, 401-426 (2013).
38. Gerstgrasser, A. et al. Cell-specific Activation of the Nrf2 Antioxidant Pathway Increases Mucosal Inflammation in Acute but Not in Chronic Colitis. J Crohns Colitis 11, 485-499 (2017).
39. Zhang, X., Chen, X., Song, H., Chen, H.Z. & Rovin, B.H. Activation of the Nrf2/antioxidant response pathway increases IL-8 expression. Eur J Immunol 35, 3258-3267 (2005).
40. Sporn, M.B. & Liby, K.T. NRF2 and cancer: the good, the bad and the importance of context. Nat Rev Cancer 12, 564-571 (2012).
41. Wruck, C.J. et al. Nrf2 induces interleukin-6 (IL-6) expression via an antioxidant response element within the IL-6 promoter. J Biol Chem 286, 4493-4499 (2011).
42. Descatoire, M. et al. Identification of a human splenic marginal zone B cell precursor with NOTCH2-dependent differentiation properties. J Exp Med 211, 987-1000 (2014).
43. Hammad, H. et al. Transitional B cells commit to marginal zone B cell fate by Taok3-mediated

surface expression of ADAM10. Nat Immunol 18, 313-320 (2017).
44. Moriyama, Y. et al. Delta-like 1 is essential for the maintenance of marginal zone B cells in normal mice but not in autoimmune mice. Int Immunol 20, 763-773 (2008).
45. Zhang, P., Zhao, Y. & Sun, X.H. Notch-regulated periphery B cell differentiation involves suppression of E protein function. J Immunol 191, 726-736 (2013).
46. Wakabayashi, N. et al. Regulation of notch1 signaling by nrf2: implications for tissue regeneration. Sci Signal 3, ra52 (2010).
47. Chen, Q. et al. Serum Metabolite Biomarkers Discriminate Healthy Smokers from COPD Smokers. PloS one 10, e0143937 (2015).
48. Hoffmann, R.F. et al. Prolonged cigarette smoke exposure alters mitochondrial structure and function in airway epithelial cells. Respir Res 14, 97 (2013).
49. Muller, T. & Hengstermann, A. Nrf2: friend and foe in preventing cigarette smoking-dependent lung disease. Chem Res Toxicol 25, 1805-1824 (2012).
50. Chaney, J.L. & Clark, P.L. Roles for Synonymous Codon Usage in Protein Biogenesis. Annual review of biophysics 44, 143-166 (2015).

**FIGURE LEGENDS (for main text only)**

**Figure 1. Metabolic B cell profile of HC and patients with primary antibody deficiency.**

(**a**) OCR (left) and ECAR (right) of $CD19^+$ B cells from HC (n = 15) and patients with primary antibody deficiency (PAD) (n = 14). (**b**) C-reactive protein (CRP) measurement over time (black line) and clinical symptoms (arrows) from patient 9 (upper). One measurement per time point. Histopathology of a skin biopsy, showing perivascular neutrophilic infiltration and nuclear debris (black arrowheads) and deposition of fibrin (red arrowheads) (lower left). Scale bar, 100 µm. Abdominal MRI scan showing a contrast enhanced soft-tissue dense area (red arrow) around the aorta, reflecting periaortitis (lower right). (**c**) Representative flow cytometry dot plots from a HC and a PPBL patient showing subset distribution of $CD19^+$ B cells stained with IgD and CD27 antibodies. Experiments were performed with 3 independent donors (**d**) Baseline OCR and ECAR measurements (T0) of primary total B cells and MZ-like B cells from HCs (each n = 4) and primary B cells from PPBL patients (n = 3) following mitochondrial perturbation with oligomycin (Oli), FCCP, and rotenone (Rot). Representative OCR/ECAR profiles of 6 independent experiments (left), and summary bar graphs of basal OCR/ECAR (right). Follow-up measurements of OCR and ECAR one year after baseline assessment (= T12) of primary B cells from HCs (n = 4) and primary B cells from PPBL patients (n = 3) (lower). Representative OCR/ECAR profiles of 3 independent experiments (lower left), and summary bar graphs of basal OCR/ECAR (lower right). (**e**) Mitochondrial perturbation profiles of primary B cells from a HC, and from PPPBL Patient 9 before (upper) and during sirolimus (2 mg/d) treatment of the patient (lower). OCR of each individual was measured once per time point and performed in triplicate. (**f**) ECAR measurements of primary B cells from HCs (n = 3) and PPBL patients (n = 3) before and following injection of IL-21+CD40L directly into the metabolic flux analyzer (dashed line). ECAR profile is representative of 3 independent experiments (left), summary bar graphs of glycolytic switch indicating area under the curve (AUC) post-activation (right). (**g**) Flow cytometry histogram, reflecting glucose (2-NBDG) uptake of primary B cells from HCs (n = 3) and PPBL patients (n = 3) activated with IL-21 plus CD40L for 24 hours prior to analysis. Shown data are representative of 3 independent experiments (left), respectively, are summarized in bar diagram (right).

Data are represented as mean ± SEM. Statistical significance was assessed by one-way ANOVA (**a**), or two-sided unpaired t-test (**d**-**g**). * $p < 0.05$, ** $p < 0.01$, *** $p < 0.001$, **** $p < 0.0001$, ns, not significant. See also **Figure S1**.

**Figure 2: Activity of individual mitochondrial respiratory chain complexes in PPBL B cells.**

(**a**) Activity-assays for CI, CII, CIV, and CV, depicted as changes in absorbance over time, comparing B-LCLs derived from HC (n = 3) and PPBL (n = 3) B cells. Graphs are representative of 4 independent experiments (left), and summarized in bar graphs (right). (**b**) OCR measurements of permeabilized B-LCLs from HCs (n = 4) and PPBL patients (n = 3) prior to and following addition of complex specific substrates as indicated (dashed lines). Data are shown as OCR graphs (left) representative of 4 independent experiments, and summary bar

graphs of complex specific OCRs (right). (**c**) OCR measurements of permeabilized B-LCLs of HCs (n = 3) and PPBL patients (n = 3), prior to and following addition of succinate, ADP and rotenone or inhibitors, as indicated (dashed lines). OCR graphs are representative of 2 independent experiments (left), and summarized as bar graphs (right). (**d**) Representative immune blot analysis (left) and quantification (right) of isolated mitochondria from B-LCLs of HCs (n = 4) and PPBL patients (n = 3) probed for Grim19, SDHA, and Tom20.
Pooled data are represented as mean ± SEM. Statistical significance was assessed by two-sided unpaired t-test (**a-d**). * $p < 0.05$, ** $p < 0.01$, ns, not significant. See also **Figure S2**.

**Figure 3: Metabolic characterization of PPBL B cells.**

(**a**) Fold change in glycolysis and TCA cycle metabolites between primary B cells from PPBL patients (n = 3) and primary MZ-like B cells from HCs (4 samples pooled of n = 7 donors). Significantly different metabolites are shown in color, with the fold change color-coded from light to dark blue (left). Bar graphs of relative abundance of glycolysis and TCA cycle metabolites (right). (**b**) Abundance of succinate and fumarate in EBV immortalized cells derived from MZ-like B cells from HCs (n = 3) and B cells from PPBL patients (n = 3). (**c**) Ratio of the abundance of α-ketoglutarate (α-KG) over (succinate + fumarate), and fumarate over succinate, both in primary MZ-like B cells from HCs and primary B cells from PPBL patients (donors as in (a)). (**d**) Metabolic tracing analysis of primary B cells from PPBL patients (n = 3) incubated for 6 hours with $^{13}$C-glucose or $^{13}$C-glutamine. Bar graphs show distribution of mass isotopologues, the scheme depicts the primary labeling of glucose- and glutamine-derived $^{13}$C fueling into the TCA cycle.
Pooled data are shown as mean ± SEM. Statistical significance was assessed by two-sided Welch's two-sample t-test, minima, maxima (box) mean (horizontal line) (**a**), two-sided unpaired t-test (**b**,**c**). * $p < 0.05$, *** $p < 0.001$, ns, not significant.

**Legend to Figure 4: Transcriptional profile of PPBL B cells.**

(**a**) Hierarchical clustering (heatmap) of sample correlation (left), and MA plot of transcriptome data (right) from primary MZ-like B cells of HCs (n = 4) and primary B cells from PPBL patients (n = 3). (**b**) mRNA abundance of MZ-like B cell marker (donors as in (a)). (**c**) Heatmap of relative expression of genes encoding complex II (donors as in (a)). (**d**) Gene set enrichment analysis of inflammatory-response genes (left) and IL-6-Jak-Stat3 pathway genes (right) (donors as in (a)). ES = enrichment score. (**e**) Heatmap of relative expression of mRNA encoding for IL-8, IL-1β, CCL5, IL-6 and TNF (donors as in (a)). (**f**) Production of IL-6 and IL-8 protein by MZ-like B-LCLs from HCs (n = 3) and B-LCLs from PPBL patients (n = 3) untreated or treated for 48 hours with IL-21+CD40L. Data are pooled from 3 independent experiments. (**g**) Quantification of IL-6 protein in the serum of PPBL patient 8. Measurements were performed on two separate occasions. Dashed line = reference value (< 3.1 ng/l)

Pooled data are shown as minima, maxima (box), mean (horizontal line) (**b**) and mean ± SEM (**f**). Statistical significance was assessed by two-sided unpaired t-test (**f**). * $p < 0.05$, ** $p < 0.01$. See also **Figure S3**.

**Legend to Figure 5: SDHA activity and inflammatory cytokine production.**

(**a**) Representative mitochondrial perturbation profile of B-LCLs from a PPBL patient untreated or incubated with the SDHA inhibitor 3-nitropropionic acid (3-NPA) for 12 hours prior to the experiment. The bar graph summarizes basal mitochondrial respiration of B-LCLs from PPBL patients (n = 3) (left). Representative mitochondrial respiration profile of permeabilized B-LCLs from a PPBL patient prior to and following addition of complex II specific substrates (succinate, ADP, malonate) as indicated (dashed lines). B-LCLs were untreated or exposed to 3-NPA for 12 hours prior to the assay. The bar graph summarizes changes in complex II OCR of B-LCLs from PPBL patients (n = 3) (middle). Quantification of IL-6 production by B-LCLs from PPBL patients (n = 3). Cells were non-activated or activated with IL-21 plus CD40L, in the presence or absence of 3-NPA for 48 hours. Data are representative of 3 independent experiments. (right). (**b**) Immunoblot analysis of B-LCLs from PPBL patients transfected with control siRNA, or *SDHA* siRNA, and probed for SDHA protein abundance. The bar graph summarizes knockdown efficiency in B-LCL from PPBL patients (n = 3) of 3 independent experiments (left). Representative data and quantification of mitochondrial respiration profile of permeabilized B-LCLs from PPBL patients (n = 3) prior to and following addition of complex II specific substrates as indicated (dashed lines). B-LCLs were treated with either control siRNA or *SDHA* siRNA prior to the assay (middle). IL-6 was quantified in the supernatant of B-LCLs from PPBL patients (n = 3), transfected with control siRNA or *SDHA* siRNA, and cultured for 48 hours. Each patient cell line was tested 3 times (right). (**c**) Immunoblot analysis of marginal zone-like B-LCLs from HCs (n = 3) transfected with control siRNA, or fumarate hydratase (FH) siRNA, and probed for FH protein abundance. Shown data are representative of 3 independent experiments (left), respectively, are summarized in bar diagram (middle). IL-6 was quantified in the supernatant of both cell populations after 48 hours of cell culture (right). (**d**) Representative data (left) and quantification (middle) of complex II specific respiration of SDHA WT and SDHA (A45T) in marginal zone-like B-LCLs from HC. IL-6 was quantified in the supernatant of both cell populations after 48 hours of cell culture (right). Data are representative for 3 independent experiments. (**e**) Time per interaction between SDHA and SDHB, calculated as area under the curve (AUC), of each individual simulation replica (n=12) (WT vs. A45T). (**f**) Molecular representation of the 'SDHA (green) SDHB (blue)' complex, shown in ribbons. The prosthetic group flavin adenine dinucleotide (FAD) is shown as sticks and CPK colored (black arrowhead). Residues of the N-ter of SDHA within 2.5 Å of SDHB are shown as sticks and CPK colored.

Pooled data are shown as mean ± SEM. Statistical significance was assessed by two-sided paired t-test (**a**, **b**), and one-way ANOVA (**e**). * $p < 0.05$, ** $p < 0.01$, *** $p < 0.001$. See also **Figure S4**.

**Legend to Figure 6: Fumarate accumulation, KEAP1–Nrf2 activity and IL-6 production.**

(**a**) Representative immunoblot analyses probing primary B cells of HC and PPBL patients for S-(2-succino)cysteine (2SC), followed by stripping and re-staining for KEAP1. The bar graph represents quantification of 2SC abundance in primary B cells of HCs (n = 3) and PPBL patients (n = 3). (**b**) Representative immunoblots of endogenous KEAP1 immunoprecipitated from Patient 1 and HC B-LCLs. Blots were probed with KEAP1 or 2SC antibodies (n = 1). (**c**) Representative imaging flow cytometry images of primary bulk B cells from a HC and a PPBL patient. Cells were stained for KEAP1 (red) and a nuclear marker (DAPI, purple). Histograms depict similarity dilate scores of KEAP1 nuclear localization in all cells analyzed (n = 1) (**d**) Phosphorylation of p62 was assessed by immunoblotting both in non-activated and activated PPBL (n = 3) and HC MZ-like (n = 3) B-LCLs. Summary bar graphs and representative blot is shown (left). Production of IL-6 by B-LCLs from PPBL patients (n = 3) treated with K67 or with DMSO in the presence or absence of IL-21+CD40L for 48 hours (right). Each patient cell line was independently tested 3 times. (**e**) Representative immunoblots (left) and quantification (right) of Nrf2 nuclear abundance from B-LCLs derived from HC MZ-like B cells (n = 3) or PPBL B cells (n= 3). (**f**) Quantification of IL-6 production by B-LCLs from PPBL patients (n = 3). Cells were non-activated or activated with IL-21 plus CD40L, in the presence or absence of the Nrf2 inhibitor, ML-385 or with vehicle (DMSO) for 48 hours. Data are pooled from 3 independent experiments. (**g**) Representative immunoblot analysis of Nrf2 protein abundance in B-LCLs of a PPBL patient transfected with control or *NRF2* si-RNA (lower left). The bar graph summarizes knockdown efficiency of B-LCLs from PPBL patients (n = 3) (upper left). IL-6 mRNA and protein (supernatant) was quantified in both cell populations after 48 hours of culture (right). Each patient cell line was independently tested 3 times. (**h**) Binding of Nrf2 to the IL-6 gene promoter (two predicted binding sites: Tbl. S3) (left), and the NQO1 and HMOX1 gene promoters (right) in primary PPBL B cells (n = 3) and HC marginal zone-like B cells (n = 2). (**i**) CRP and BSR measurements before and after IL-6 receptor blockade (left). Result of the patient questionnaire filled by the patient (right).

Pooled data are shown as mean ± SEM. Statistical significance was assessed by two-sided unpaired t-test (**a**,**e**,**h** (right panel)), Wilcoxon signed rank test (**f**), two-sided paired t-test (**d**,**g**), and two-way ANOVA (**h**, left panel). * $p < 0.05$, ** $p < 0.01$, ns, not significant. See also **Figure S5**.

## METHODS

### Study subjects

The study was approved by the *Ethikkommission Nordwest- und Zentralschweiz* (EKNZ 2015-187); complied with all relevant ethical regulations, and informed consent was obtained from all participants. Fourteen patients, and 15 age and sex matched HC, were prospectively recruited between July 2015 and December 2016. One additional PPBL patient was recruited 2018. Inclusion criteria for patients were as follows: Age >18 years; serum IgG level <7g/l, or IgG subclass deficiency ($IgG_1$ <4.9 g/l, $IgG_2$ <1.5 g/l, $IgG_3$ <0.2 g/l, $IgG_4$ <0.08 g/l). Patients evaluated by a Clinical Immunologist and classified as having a form of secondary antibody deficiency were excluded from the study.

### Blood sample routine phenotyping and immunoglobulin quantification

After written informed consent, blood samples from patients and HC (Blood donor Center, University Hospital Basel) were obtained. From all patients a differential white blood cell count, including total lymphocyte as well as T and B cell absolute numbers, were obtained. B cells ($CD19^+$ in lymphocyte gate) were further phenotyped as follows: naïve B cells ($IgD^+CD27^-IgM^+$), marginal zone-like B cells ($IgD^+CD27^+IgM^+$), memory B cells ($IgD^-CD27^+IgM^-$), transitional B cells ($IgD^+IgM^+CD38^+$), CD21 low B cells ($CD21^{low}CD38^-$), and plasmablasts ($IgD^-IgM^-CD38^{++}$). T cells ($CD3^+$ in lymphocyte gate) were classified into: $CD4^+$ T cells, $CD8^+$ T cells, naïve ($CD27^+CD45RO^-$) vs. central memory ($CD27^+CD45RO^+$) vs. effector memory ($CD27^-CD45RO^{+/-}$). Serum levels of total IgG and IgG subclasses ($IgG_{1-4}$); IgM; IgA (data not shown), and IgE (data not shown) were quantified. All above experiments were performed at the accredited Medical Immunology Laboratory (ISO 17025) of the University Hospital Basel.

### Cell sorting and phenotyping

Peripheral blood mononuclear cells (PBMCs) were isolated by standard density-gradient centrifugation (Lymphoprep Fresenus Kabi, Norway). B cells ($CD19^+$) and T cells ($CD3^+$) were positively selected using magnetic beads (Miltenyi Biotec, Germany) according to the manufacturer's instructions. For isolation of marginal zone-like B cells, B cells ($CD19^+$) were stained with anti-CD27 brilliant Violet 605 (O323) (Biolegend, USA) and anti-IgD VioBlue (REA740, Miltenyi Biotec) mAb. $CD19^+$ $CD27^+$ $IgD^+$ B cells were sorted with a BD Influx cell sorter (BD Bioscience, USA). FACS sorted naïve and memory B cells (as above) were activated with CpG (2.5 μg/ml) for 24 hours and then stained with anti-CD86-PE (IT2.2, Biolegend), anti-CD69-FITC (FN50, Immunotools), anti-HLADR-APC (G46-6, BD Biosciences), and anti-CD71-PE (CY1G4, Biolegend). For carboxyfluorescein succinimidyl ester (CFSE) dilution assays, PBMCs were stained with CFSE and then activated with anti-CD3 and anti-CD28 mAb (for T cells), or with CpG or IL-21/CD40L (for B cells). Cells were stimulated for 5 days and then assessed by flow cytometry. For CMV

ELISPOT assays patient and HC PBMCs were stimulated CMV antigens using the T-track CMV kit (Lophius). For detailed B cell phenotyping the following additional antibodies were used: anti-CD24 (IML5, Biolegend), anti-CD38 (HIT2, BD Biosciences), anti-TACI (1A1, Biolegend).

**EBV transformed B lymphocyte cell lines**

PBMCs or sorted marginal zone-like B cells were incubated with EBV-containing supernatant from B95-8 cells for 1 hour and additionally stimulated with CpG (1 µg/ml). Cyclosporine A (1 µg/ml) was added weekly for a total of four weeks to eliminate T cells. Purity of EBV transformed B cell lines, as defined by flow cytometry, was 92-98 % ($CD19^+$ $CD3^-$).

**Metabolic flux analysis**

A Seahorse XF-96$^e$ extracellular flux analyzer (Seahorse Bioscience, Agilent Technologies, USA) was used to define oxygen consumption rates (OCR) and extracellular acidification rates (ECAR). Mitochondrial perturbation experiments were carried out by sequential addition of oligomycin (1 µM, Sigma-Aldrich, USA), FCCP (2 µM, Carbonyl cyanide 4-(trifluoromethoxy) phenylhydrazone, Sigma-Aldrich), and rotenone (1 µM, Sigma-Aldrich). For measuring activation-induced glycolytic activity, primary B cells were activated with IL-21 (200 ng/ml, ImmunoTools, Germany) and CD40L (200 ng/ml, Sigma-Aldrich) injected into the metabolic flux analyzer via injection ports, and ECAR was monitored in real time. For monitoring OCR of intact mitochondria only, cells were resuspended in MAS buffer (70 mM sucrose, 220 mM mannitol, 10 mM $KH_2PO_4$, 5 mM $MgCl_2$, 2 mM HEPES, and 1 mM EGTA), then treated with the XF plasma membrane permeabilizer (Seahorse, Agilent Technologies), which was followed by addition of pyruvate (5 mM) / malate (2.5 mM) / ADP (1 mM) and rotenone (1 µM) for monitoring complex I-driven respiration; succinate (10 mM) / ADP (1 mM) with/without rotenone (1 µm / 2 µm) and malonate (0.04 mM) for monitoring complex II-driven respiration; duroquinol (0.5 mM) / ADP (1 mM) and antimycin A (0.02 mM) for monitoring complex III-driven respiration; TMPD (0.5 mM) / Ascorbate 2 mM) / ADP (1 mM) and sodium azide (20 mM) (all from Sigma-Aldrich) for monitoring complex IV-driven respiration. Changes in OCR upon substrate addition were calculated relative to the pre-injection rate.

**2-NBDG uptake**

To assess glucose-uptake, $5x10^5$ primary B cells were activated with IL-21 (200 ng/ml, ImmunoTools) and CD40L (200 ng/ml, Sigma-Aldrich) for 24 hours. Cells were then incubated in medium containing 20 µM 2-NBDG (Invitrogen) for 45 min and analyzed by flow cytometry.

**Electron microscopy**

Transmission electron microscopy was performed at the Biozentrum (University of Basel). Primary B cells were sequentially fixed in 3% paraformaldehyde, 0.5% glutaraldehyde and 1% osmium tetraoxide, embedded and then cut into 60 nm sections. Micrographs (27'000x magnification) were obtained with a Morgagni 268 (FEI, Hillsboro OR, USA) transmission electron microscope operated at 80 kV. ImageJ software (NIH, Bethesda, USA) was used for measuring cell area; mitochondrial area, and mitochondrial length (major axis) and width (minor axis). The aspect ratio of mitochondria was calculated as 'major axis' over 'minor axis', an aspect ratio of 1 indicating a circular mitochondrial section.

**Isolation of mitochondria**

Cell pellets were washed with cold PBS and lysed using RIPA buffer (Thermo Fisher Scientific, Rockford IL, USA) containing protease and phosphatase inhibitors (Roche, Switzerland). To prepare mitochondrial fractions, $3x10^7$ B-LCLs were collected and washed with buffer A (83 mM sucrose, 10 mM MOPS, pH 7.4). Cell pellets were then homogenized with 20 strokes in a tightly fitting glass-teflon homogenizer with 1 ml of buffer B (buffer A plus 10mM triethanolamine, 5% percoll, 0.01% digitonin, protease inhibitor, pH 7.4). Nuclei and unbroken cells were removed by centrifugation at 2'500 x *g* for 5 min. Supernatants were collected and centrifuged at 10'000 x *g* for 15 min. Mitochondria were then suspended in an appropriate volume of buffer C (300 mM sucrose, EGTA 1 mM, 20mM MOPS, protease inhibitor, pH 7.4) for storage at −80°C until use.

**Immunoblot analysis**

Whole-cell lysates or mitochondrial fractions were separated by 4-15% Mini Protean TGX Gel (Bio-Rad, Hercules CA, USA), and transferred to nitrocellulose using Trans-Blot Turbo Transfer (Bio-Rad, Hercules CA, USA). Membranes were probed with anti-Grim19 mAb (ab110240), anit-NDFU8 mAb (ab110242), anti-SDHB mAb (ab14714), anti-Complex III subunit Core 2 mAb (ab14745), anti-Complex IV subunit II mAb (ab110258), anti-ATPα mAb (ab14748), anti-ATP5A mAb (ab176569), Anti-UQCRC2 mAb (ab14745), anti-MTCO2 mAb (ab110258) and anti-Tomm20 mAb(ab56783)(all from Abcam), anti-SDHA mAb (119989), anti-FH mAb (4567), anti-KEAP1 mAb (8047), anti-Nrf2 pAb (12721), pan-methyl-histone H3 (Lys9) mAb (4473) and anti-β-actin mAb (3700) (all from Cell Signaling, USA) and anti-2SC pAb (crb2005017e, Cambridge Research Biochemicals, UK). Blots were then stained with the appropriate secondary antibody (IRDye 800CW-conjugated goat polyclonal antibody against rabbit IgG (926-32211) or RDye 800CW-conjugated goat polyclonal antibody against mouse IgG (926-32219) from LI-COR). The Odyssey imaging system (LICOR) was used for detection, and the ImageJ software (1.48v) for quantification.

**Blue native PAGE**

For isolation of mitoplasts, 8 x $10^6$ B-LCLs were re-suspended in 100 µl of PBS, 32.5 µl of digitonin (8 mg/ml) was added and cells were incubated on ice for 10 min. Cold PBS (1 ml) was added and cells were centrifuged for 5 min at 10'000 x *g*. The pellet was resuspended in 100 µl of AA buffer (500 mM 6-aminohexanoic acid, 50 mM immidazole, 1 mM EDTA, pH 7) and 10 µl of a 10% digitonin solution was added. Next, cells were centrifuged for 30 min at 18'000 x *g*. Supernatant was harvested and 10 µl of sample buffer (5% blue G-250, 5% glycerol in AA Buffer) was added. BN-PAGE was performed as described[51]. Membranes were probed for anti-NDUFA9 mAb (20C11B11B11, Abcam), anti-complex II 70 kDA Fp mAb (459200, Invitrogen), Anti-UQCRC1 mAB (16D10AD9AH5) (110252, Abcam), anti-oxphos Complex IV Subunit I mAb (459600, Invitrogen), anti-ATPB antibody [3D5] - Mitochondrial Marker mAb (14730, Abcam) and Tomm20 (FL-145) (sc11415, Santa Cruz Biotechnology, USA).

**Mitotracker red and mitotracker deep red staining**

Primary B cells were incubated for 20 min at 37°C / 5% $CO_2$ with 100 nM Mitotracker red (MTR, Invitrogen), or 100 nM Mitotracker deep red (MTDR, Invitrogen), respectively. Cells were then washed twice in staining buffer (PBS plus 1% bovine serum albumin) and analyzed by flow cytometry.

**Activity of individual respiratory chain complexes**

To measure the activity of individual mitochondrial respiratory chain complexes, ELISA microplate assay kits (Abcam, UK) were used according to the manufacturer's instructions.

**Metabolomics**

Cells from primary patient B cells and primary marginal zone-like B cells from HC were isolated as described above, washed twice with cold PBS, snap frozen in EtOH containing dry ice and stored at −80°C. Metabolomic assays and analysis were performed by Metabolon Inc. (Durham, USA). Importantly, the settings used enabled the separation of methylmalonate from the isobaric succinate. The two metabolites succinate and fumarate were analyzed by electrospray ionization in the negative mode using multiple reaction monitoring. Metabolomics data can be accessed under: www.ebi.ac.uk/metabolights/MTBLS1137

**$^{13}C_6$ glucose and $^{13}C_6$ glutamine tracing**

Primary B cells (2x$10^6$) from patients were plated onto 48 well plates in RPMI10-FBS with 4 mM U-$^{13}$C glucose or 4 mM U-$^{13}$C glutamine for 6 hours. Metabolites were extracted with 50 % MeOH / 30 % Acetonitrile. Isotopologue distribution was assessed by GC-MS. Metabolites were extracted from cells

using ice-cold 80 % methanol, followed by sonication and removal of cellular debris by centrifugation at 4°C. Metabolite extracts were dried, derivatized as tert-butyldimethylsilyl (TBDMS) esters, and analyzed via GC-MS. Uniformly deuterated myristic acid (750 ng / sample) was added as an internal standard following cellular metabolite extraction, and metabolite abundance was expressed relative to the internal standard, and normalized to cell number. Mass isotopomer distribution was determined using a custom algorithm developed at McGill University, Canada[52].

**RNA sequencing**

RNA from primary patient B cells and primary marginal zone-like B cells from HC was isolated using nucleospin RNA kit (Macherey-Nagel, Germany) following manufacturer's instructions. RNA-seq was performed by Admera Health (USA). Obtained single-end RNA-seq reads were mapped to the human genome assembly, version hg38 (analysis set, downloaded from UCSC https://genome.ucsc.edu), with RNA-STAR, with default parameters except for reporting for multi-mappers only one hit in the final alignment files (outSAMmultNmax=1) and filtering reads without evidence in spliced junction table (outFilterType="BySJout")."). All subsequent gene expression data analysis was done within the R software (R Foundation for Statistical Computing, Vienna, Austria). Raw reads and mapping quality was assessed by the qQCreport function from the R/Bioconductor software package QuasR (version 1.18.0). Using Ensembl Genes mRNA coordinates from ensembl version 88 (https://www.ensembl.org) and the qCount function from QuasR package, we quantified gene expression as the number of reads that started within any annotated exon of a gene. Only genes with valid Entrez Gene Id were kept. The differentially expressed genes were identified using the edgeR package (version 3.20.9)[53]. RNA seq data can be accessed under the GEO accession number (GSE135173).

**Whole exome sequencing**

The Oragene DNA OG-500 kit (DNA Genotek Inc., Canada) was used to collect saliva from patients, DNA was extracted using PrepIT L2P reagent (DNA Genotek Inc.). Sonication as well as library preparation was performed using the SureSelectXT Target Enrichment System for Illumina Paired-End Sequencing Library Protocol (Version C0, December 2016). SureSelectXT Reagent kits were used for library preparation (Agilent Technologies). Exon-specific biotinylated oligonucleotides, SureSelect Human All Exon V6 (Agilent Technologies), were hybridized with the samples. Exons were pulled down using Dynabeads MyOne Streptavidin T1 magnetic beads (Thermo Fisher Scientific). Paired-end 125 bp sequencing was performed on HiSeq 4000 Illumina platform. Output files from the sequencer were in FASTQ format. Paired-end sequencing resulted in two FASTQ files for each sample, forward and reverse. Forward and reverse FASTQ files were aligned to the reference genome (hg19) using Burrows-Wheeler

Aligner. The output of BWA was a sequence alignment map (SAM) file. Picard tools v2.7.1 was used to make a binary version of SAM files (=BAM files). Quality control was performed as per Genome Analysis Tool Kit (GATK) v3.5 guidelines from Broad Institute[54]. Each output BAM file was individually analyzed for variants from the reference genome using HaplotypeCaller from GATK resulting in a variant called file (VCF). Annotation of mutations was performed using Combined Annotation Dependent Depletion (CADD v1.3) and Variant effect predictor (VEP) programs. Mutations of interest were visualized *in silico* using the Integrative Genomics Viewer (IGV) in order to confirm the mutation was in fact somatic and not present in controls. The synonymous mutation was further investigated for splice altering, miRNA site, or mRNA structure altering, using NNSplice, Human Splicing Finder, TargetScan and Rescue ESE[55, 56]. Somatic analysis was performed using VarScan v2.3.9 (ref [57]), Strelka Somatic Caller and MuTect2 (refs. [58, 59]). Annotation of somatic mutations from the 3 callers was performed using CADD v1.3 and VEP programs. The WES data can be accessed under the BioProject number PRJNA557194 (https://www.ncbi.nlm.nih.gov/sra/PRJNA557194).

**Cytokine measurements**

B-LCLs (4 x $10^6$) from patients, and marginal zone-like B-LCLs from HC, were plated into 48 well plates. Cells were either left unstimulated (non-activated controls), or activated with IL-21 (40 ng/ml, ImmunoTools) and CD40L (40 ng/ml, Sigma-Aldrich). As indicated, 3-NPA (1.5 μM, Sigma-Aldrich), ML-385 (5 μM, Sigma-Aldrich), SML-1922 (50 μM, Sigma-Aldrich) or monomethyl fumarate (25 μM) was added. Supernatants were harvested 48 hours after activation, and concentrations of IL-6 was measured using Legendplex, human multiplex Panel (Biolegend), according to the manufacturer's instructions.

**RNA mediated interference**

B-LCLs (2x$10^6$) from patients, and marginal zone-like B-LCLs from HC, were transfected with pools of siRNA targeting *SDHA*, *NRF2*, or control scrambled siRNA (each 30 pmol) (QIAGEN) and rested for 48 hours, using the AMAXA cell line V nucleofection kit (Lonza). Knockdown efficiency was assessed by immunoblot analyses of the respective proteins.

**CRISPR-editing**

Introduction of the SDHA A45T point mutation into B-LCLs from HC marginal zone-like B cells was performed by Genoway.

**Molecular dynamics simulation**

Interaction between SDHA and SDHB were studied using MD simulations. To date no structures of human SDHA or SDHB have been published, yet the crystal structure of porcine heart mitochondrial complex II has been solved at 3.1 Å resolution (PDB code 4YTP)[60]. To generate a model of the human SDHA/SDHB complex, the sequence of the protein, as obtained from the US National Centre for Biotechnology Information (https://www.ncbi.nlm.nih.gov - accessed 22nd February 2018), was submitted to the automated protein structure homology-modeling server, SWISS-MODEL[61]. Using the VMD[62] and Chimera suites[63], a complex of human SDHA and SDHB was designed. Two different models were generated, each extended at the N-ter with segments of sequence ASAKVSDSI (wt) and ASTKVSDSI (A45T mutation), respectively[62, 64]. The structure of FAD was obtained from the Zinc library and their parameters were calculated through the CHARMM General Force Field (CGenFF) version 1.0.0[65]. Simulations were conducted with the GROMACS package, version 2016.3[66], using parallel tempering. The CHARMM36 topology and parameter files were used to represent the protein and water was represented by the TIP3P model, whereas parameters for FAD were calculated with CGenFF[65]. Isotropic pressure at 1 bar was virtually maintained through coupling to a Parrinello-Rahman barostat[67], with a virtual compressibility of 4.5 x $10^{-5}$ bar and a coupling time of 5 ps. For parallel tempering, an ensemble of 48 temperatures in the range 310-385K was generated, whereas solute and solvent were weakly coupled to Nose-Hoover[68] thermostats with coupling times of 1 ps[69]. Each individual trajectory was ~22.5-23.0 ns long, totalizing 1100 and 1080 ns for the wt and the A45T mutant, respectively. The trajectories simulated for at a temperature lower than 360K were retained for the analyses, which were conducted either on the statistical platform R and specific R packages, GROMACS tools, or in-house Python scripts[70].

**_SDHA_ end point PCR and sequencing**

RNA was isolated from B-LCL (5 x $10^6$) of patient #8 using Trizol (Thermo Fisher Scientific) and chloroform (Sigma-Aldrich) according to the manufacturer's protocol, then purified with the QIAamp RNA Blood Mini Kit (QIAGEN, Germany). Random primers (Promega, USA) were annealed at 70°C for 5 min. cDNA synthesis was performed according to the Qiagen's GoScript Reverse Transcription System protocol in a TProfessional TRIO PCR Thermocycler (Core Life Sciences, USA). To search for the mutation in the cDNA of patient #8, primers were designed to amplify a fragment of the *SDHA* transcripts by using the ncbi primer blast web tool (https://www.ncbi.nlm.nih.gov/tools/primer-blast/). The following primers were used: Forward primer: CGA CTC CGG CGT GGT G; Reverse primer: TTT TCT AGC TCG ACC ACG GC. End point PCR was performed using cDNA of B-LCL from patient #8, and Go Taq G2 DNA Polymerase (Promega) with the GoTaq Green Master Mix (Promega) in a TProfessional TRIO PCR Thermocycler (Core Life Sciences). PCR products were separated using a 1.5% agarose gel

electrophoresis and the band around the expected length of 534 bp was extracted and purified using Qiaquick Gel Extraction Kit (QIAGEN). Extracted DNA was used for Sanger sequencing.

**SDHA plus SDHB activity**

SDH activity (i.e. compound activity of SDHA and SDHB) was measured spectrophotometrically from the reduction of 2,6-diclorophenol-indophenol (DCPIP) by tracking the absorbance at 600 nm over 3 min. Specifically, frozen B-LCLs (5 x $10^6$) were thawed and resuspended in 100 µl PBS on ice, protein concentration was determined, and the volume was adjusted to the sample with the lowest concentration. Each sample (20 µl) was suspended in 950 µl of buffer C1/C2 (25 mM potassium phosphate ($K_2HPO_4$) (pH = 7.2), 5 mM $MgCl_2$, 3 mM KCN, 2.5 mg/ml BSA) supplemented with 100 mM succinate and 0.1% Triton X-100, and incubated 10 min at room temperature. After addition of 6 µl 5 mM DCPIP, 2 µl 1 mg/ml of antimycin A and 2 µl 1 mM rotenone, samples were incubated for 2 min. Then, 6 µl of 10 mM phenazine methosulfate (PMS) was added and absorbance was measured. Compound activity of SDHA and SDHB was extrapolated using the following formula: [SDH activity = ((rate/min)/19.1) / sample volume x 1000 x dilution factor], where 19.1 is the molar extinction coefficient at 30°C ($mM^{-1}$ $cm^{-1}$).

**Overexpression**

B-LCLs were nucleofected (Lonza) with Flag-KEAP1 for 24 or 48 hours. Flag-KEAP1 was a gift from Qing Zhong (UC Berkeley). KEAP1 interacting proteins were purified using anti-FLAG antibodies (clone 9A3, Cell signaling) and identified by affinity purification MS. Transfection efficiency was assessed by Immunoblots.

**Imaging Flow cytometry**

Primary B cells from HC and PPBL patients were fixed with 4% paraformaldehyde and permeabilized with 0.3% Triton-X 100. Cells were blocked with 5% goat serum and stained with primary antibody (Keap1-mAb Ms, Thermo-Fisher; Nrf2-pAb Rb, Abcam) in blocking medium at 4°C, overnight. Cells were then stained with secondary antibodies (Thermo Fisher) and counterstained with DAPI. Images were acquired using the Imagestream X Mark II imaging flow cytometer (AMNIS). Between 1000-2000 events were collected and imaged at 60x magnification. For analysis, the nuclear localization wizard from the IDEAS software (AMNIS) was used. High similarity dilate mean scores reflect increased nuclear localization. For assessment of Nrf2 nuclear translocation following addition of Keap1 activation, cells were treated with K67 for 24 hours and then fixed for staining as above.

**ChIP-PCR**

ChIP-PCR was performed by Active Motif. In brief, human B cells were fixed with 1% formaldehyde for 15 min and quenched with 0.125 M glycine. Chromatin was isolated by the addition of lysis buffer, followed by disruption with a Dounce homogenizer. Lysates were sonicated using the EpiShear™ Probe Sonicator (Active Motif) with an EpiShear™ Cooled Sonication Platform (Active Motif) and the DNA sheared to an average length of 300-500 bp. Genomic DNA (Input) was prepared by treating aliquots of chromatin with RNase, proteinase K and heat for de-crosslinking (overnight at 65°C) followed by ethanol precipitation. Pellets were resuspended and the resulting DNA was quantified on a CLARIOStar® spectrophotometer. Extrapolation to the original chromatin volume allowed quantitation of the total chromatin yield. Aliquots of chromatin (25 μg) were precleared with protein A agarose beads (Invitrogen). Genomic DNA regions of interest were isolated using an antibody against NRF2 (Santa Cruz Biotechnologies, cat. no. sc-13032), Complexes were washed, eluted from the beads with SDS buffer, and subjected to RNase and proteinase K treatment). Crosslinks were reversed by incubation overnight at 65°C, and ChIP DNA was purified by phenol-chloroform extraction and ethanol precipitation. Quantitative PCR (QPCR) reactions were carried out in triplicate using SYBR Green Supermix (Bio-Rad) on a CFX Connect™ Real Time PCR system. The resulting signals were normalized for primer efficiency by carrying out QPCR for each primer pair using pooled input DNA from the samples.

Please also see accompanying *Life Sciences Reporting Summary*.

**DATA AVAILABILITY STATEMENT**

Web links for publicly available datasets are provided at the appropriate places in the manuscript, accession codes for metabolomics, RNAseq and WES data have been added to the respective methods sections. No restrictions on data availability apply. Patient material may not be available anymore. All figure panels, with exception of Figure S5G, are associated with raw data.

**REFERENCES (methods-only)**


51. Wittig, I., Braun, H.-P. & Schägger, H. Blue native PAGE. Nature protocols 1, 418-428 (2006).
52. McGuirk, S. et al. PGC-1α supports glutamine metabolism in breast cancer. Cancer & metabolism 1, 22 (2013).
53. Robinson, M.D., McCarthy, D.J. & Smyth, G.K. edgeR: a Bioconductor package for differential expression analysis of digital gene expression data. Bioinformatics 26, 139-140 (2010).
54. McKenna, A. et al. The Genome Analysis Toolkit: a MapReduce framework for analyzing next-generation DNA sequencing data. Genome Research 20, 1297-1303 (2010).
55. Agarwal, V., Bell, G.W., Nam, J.-W. & Bartel, D.P. Predicting effective microRNA target sites in mammalian mRNAs. eLife 4, 101 (2015).
56. Reese, M.G., Eeckman, F.H., Kulp, D. & Haussler, D. Improved splice site detection in Genie. Journal of computational biology : a journal of computational molecular cell biology 4, 311-323 (1997).
57. Koboldt, D.C. et al. VarScan 2: somatic mutation and copy number alteration discovery in cancer by exome sequencing. Genome Research 22, 568-576 (2012).
58. Cibulskis, K. et al. Sensitive detection of somatic point mutations in impure and heterogeneous cancer samples. Nature biotechnology 31, 213-219 (2013).
59. Saunders, C.T. et al. Strelka: accurate somatic small-variant calling from sequenced tumor-normal sample pairs. Bioinformatics (Oxford, England) 28, 1811-1817 (2012).
60. Inaoka, D.K. et al. Structural Insights into the Molecular Design of Flutolanil Derivatives Targeted for Fumarate Respiration of Parasite Mitochondria. International journal of molecular sciences 16, 15287-15308 (2015).
61. Biasini, M. et al. SWISS-MODEL: modelling protein tertiary and quaternary structure using evolutionary information. Nucleic acids research 42, W252-258 (2014).
62. Humphrey, W., Dalke, A. & Schulten, K. VMD: visual molecular dynamics. Journal of molecular graphics 14, 33-38- 27-38 (1996).
63. Pettersen, E.F. et al. UCSF Chimera--a visualization system for exploratory research and analysis. Journal of computational chemistry 25, 1605-1612 (2004).
64. Huo, X. et al. Preliminary molecular characterization and crystallization of mitochondrial respiratory complex II from porcine heart. The FEBS journal 274, 1524-1529 (2007).
65. Vanommeslaeghe, K. et al. CHARMM general force field: A force field for drug-like molecules compatible with the CHARMM all-atom additive biological force fields. Journal of computational chemistry 31, 671-690 (2010).
66. Bussi, G. Hamiltonian replica exchange in GROMACS: a flexible implementation. Molecular

Physics 112, 379-384 (2014).
67. Parrinello, M. & Rahman, A. Polymorphic transitions in single crystals: A new molecular dynamics method. Journal of Applied Physics 52, 7182-7190 (1981).
68. Hoover, W. Canonical dynamics: Equilibrium phase-space distributions. Physical review. A, General physics 31, 1695-1697 (1985).
69. Hess, B. P-LINCS: A Parallel Linear Constraint Solver for Molecular Simulation. Journal of chemical theory and computation 4, 116-122 (2008).
70. Zeileis, A. & Grothendieck, G. zoo: S3Infrastructure for Regular and Irregular Time Series. Journal of Statistical Software 14, 1-27 (2005).

## Figure S1

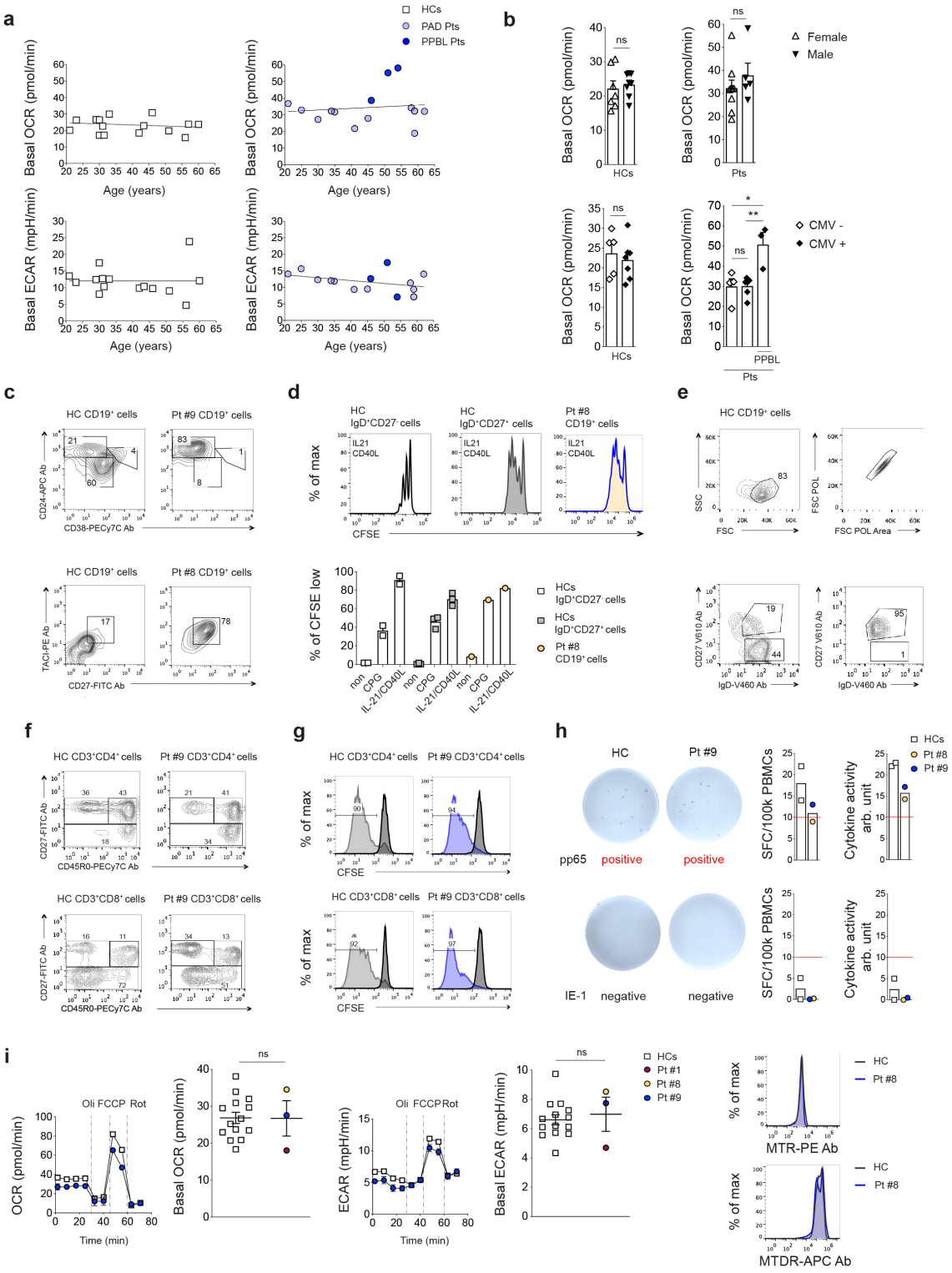
a
HCs
PAD Pts
PPBL Pts
Basal OCR (pmol/min)
Basal ECAR (mpH/min)
Age (years)
b
ns
HCs
Pts
Female
Male
CMV -
CMV +
PPBL
c
HC CD19+ cells
Pt #9 CD19+ cells
Pt #8 CD19+ cells
CD24-APC Ab
CD38-PECy7C Ab
TACI-PE Ab
CD27-FITC Ab
d
HC IgD+CD27- cells
HC IgD+CD27+ cells
Pt #8 CD19+ cells
IL21
CD40L
% of max
CFSE
% of CFSE low
non
CPG
IL-21/CD40L
HCs IgD+CD27- cells
HCs IgD+CD27+ cells
Pt #8 CD19+ cells
e
SSC
FSC
FSC POL
FSC POL Area
CD27 V610 Ab
IgD-V460 Ab
f
HC CD3+CD4+ cells
Pt #9 CD3+CD4+ cells
HC CD3+CD8+ cells
Pt #9 CD3+CD8+ cells
CD27-FITC Ab
CD45R0-PECy7C Ab
g
h
HC
Pt #9
pp65
positive
IE-1
negative
SFC/100k PBMCs
Cytokine activity arb. unit
HCs
Pt #8
Pt #9
i
Oli
FCCP
Rot
OCR (pmol/min)
Time (min)
Basal OCR (pmol/min)
ECAR (mpH/min)
Basal ECAR (mpH/min)
Pt #1
MTR-PE Ab
MTDR-APC Ab

**Supplementary Figure 1**

**Oxygen consumption rates are increased in PPBL B cells**

(**a**) Age distribution of basal OCR and basal ECAR in primary B cells from HCs (n = 15) and PAD patients (n = 14). (**b**) Basal OCR in primary B cells from female vs. male and $CMV^-$ vs. $CMV^+$ HCs (n = 13) and PAD patients (n = 14). (**c**) Representative cell surface phenotype of B cells ($CD19^+$ lymphocytes) from HCs and PPBL patients stained with CD24, CD38, TACI, and CD27 antibodies. HCs (n=2) and PPBL patients (n=2) were independently tested once. (**d**) CFSE dilution histogram of sorted $CD19^+$ $IgD^+CD27^-$; $IgD^+CD27^+$ and PPBL B cells stimulated with IL-21 and CD40L or CPG for 5 days (upper panel) and summarized in bar diagram (lower graph). Representative of 3 independent experiments. (**e**) Gating strategy for sorting MZ-like B cells from healthy controls. $CD19^+$ cells were discriminated based on SSC/FSC area (upper left) and doublets were gated out (upper right). MZ-like B cells are $IgD^+CD27^+$ cells (lower left). Sorted MZ-like B cells after FACS sorting (lower right). (**f**) Relative distribution of $CD4^+$ and $CD8^+$ T cell subsets from HCs (n=3) and a PPBL patients (n=3). Representative of 3 independent experiments. (**g**) Representative histograms of CFSE dilution assays of anti-CD3/anti-CD28 activated $CD4^+$ and $CD8^+$ T cells from a HC and a PPBL patient. Representative of 3 independent experiments. (**h**) T cell reactivity against CMV peptides (pp65 and IE-1) between HCs (n=2) and PPBL patient T cells (n=2) were assessed by IFN-gamma ELISpot. The result is positive if the geometric mean is > 10 (red line) (**i**) Representative mitochondrial perturbation profiles of primary T cells from HCs and PPBL patients. Summary graphs present basal OCR (left) and ECAR (middle) of primary T cells from HCs (n = 14) and PPBL patients (n = 3). Representative mitotracker red (MTR) and mitotracker deep red (MTDR) staining of primary B cells from HCs (n = 3) and PPBL patients (n = 3) (right). Representative of 3 independent experiments.
Pooled data are presented as mean ± SEM. Statistical significance was assessed by two-sided unpaired t-test (**b**,**h**). * $p < 0.05$, ** $p < 0.01$, ns, not significant.

## Figure S2

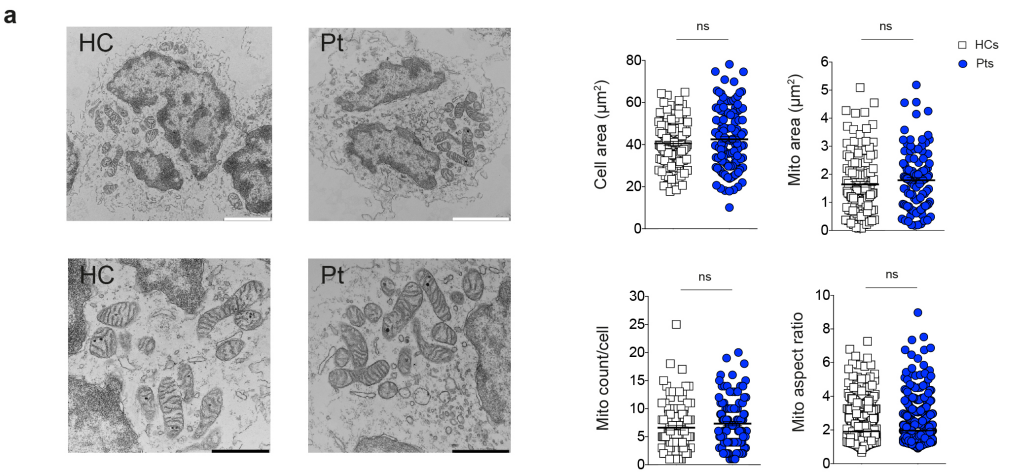
a
HC
Pt
HC
Pt
ns
Cell area (µm²)
Mito area (µm²)
Mito count/cell
Mito aspect ratio
HCs
Pts

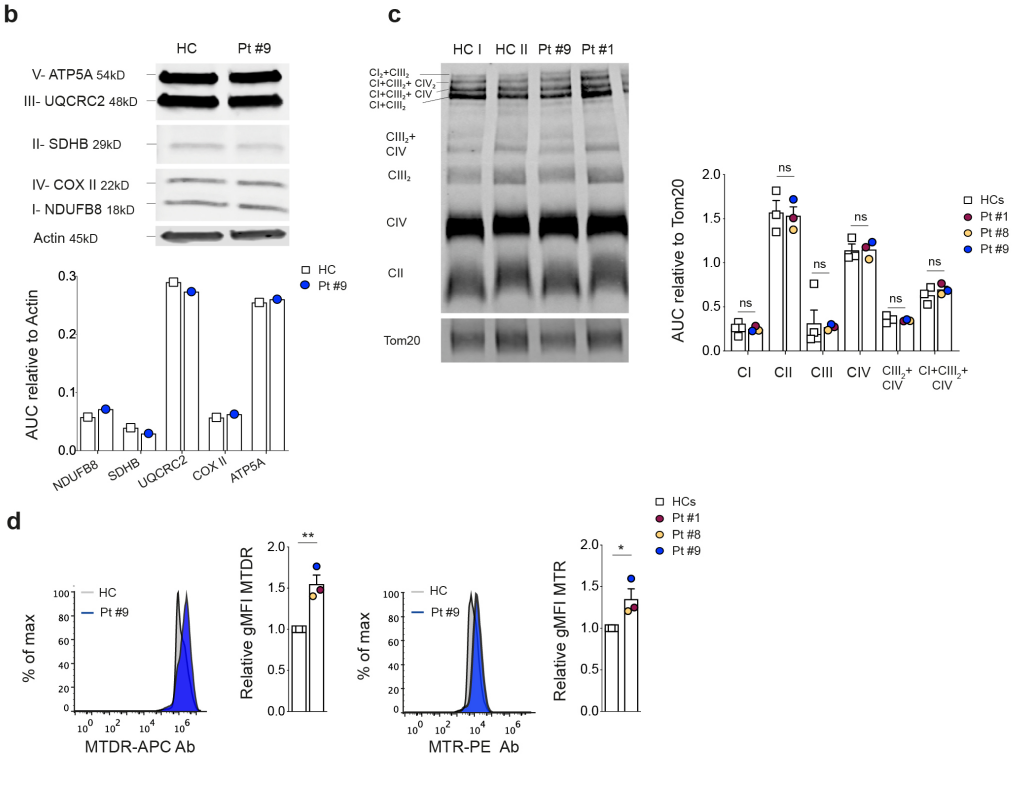
b
HC
Pt #9
V- ATP5A 54kD
III- UQCRC2 48kD
II- SDHB 29kD
IV- COX II 22kD
I- NDUFB8 18kD
Actin 45kD
AUC relative to Actin
NDUFB8
SDHB
UQCRC2
COX II
ATP5A
c
HC I
HC II
Pt #9
Pt #1
Tom20
AUC relative to Tom20
CI
CII
CIII
CIV
HCs
Pt #1
Pt #8
Pt #9
d
HC
Pt #9
% of max
MTDR-APC Ab
Relative gMFI MTDR
MTR-PE Ab
Relative gMFI MTR

**Supplementary Figure 2**

## Complex II is hyper-functional in PPBL B cells

(**a**) Representative transmission electron microscopy images of a primary B cell from a HC and a PPBL patient (left). White scale bar, 2000 nm. Black scale bar, 1000 nm. Summary graphs of cell area; mitochondrial area; mitochondria count per cell, and mitochondrial aspect ratio (length/width) from HCs (n = 3) and PPBL patients (n = 3) (right). 45 B cells were analyzed per individual in 3 independent experiments. (**b**) Representative immunoblot analysis of primary B cells from a HC and a PPBL patient. Blots were probed for Complex I (CI) subunit NDUFB8, Complex II (CII) subunit SDHB, Complex III (CIII) subunit Core 2, Complex IV (CIV) subunit I, Complex V (CV) ATP synthase subunit alpha, as well as actin (upper). Bar graph depicts quantification of the abundance of each complex subunit relative to actin (lower). Experiment was performed once. (**c**) BN-PAGE immunoblot analysis of enriched mitochondria from B-LCLs of HCs (n = 3) and PPBL patients (n= 3), probed for CI (NDUFA9), CII (SDHA), CIII (UQCRC1), CIV (subunit I) and Tom20 (left). Summary bar graph (right). Representative of 4 independent experiments. (**d**) Representative mitotracker deep red (MTDR) and mitotracker red (MTR) staining of primary B cells from HCs (n = 3) and PPBL patients (n = 3). Bar graph summarizes the geometric mean fluorescence intensity (gMFI) of MTDR and MTR of both populations.

Pooled data are represented as mean ± SEM. Statistical significance was assessed by two-sided Mann-Whitney test (**a**), two-sided unpaired t-test (**c**,**d**). * $p < 0.05$, ** $p < 0.01$, ns, not significant.

## Figure S3

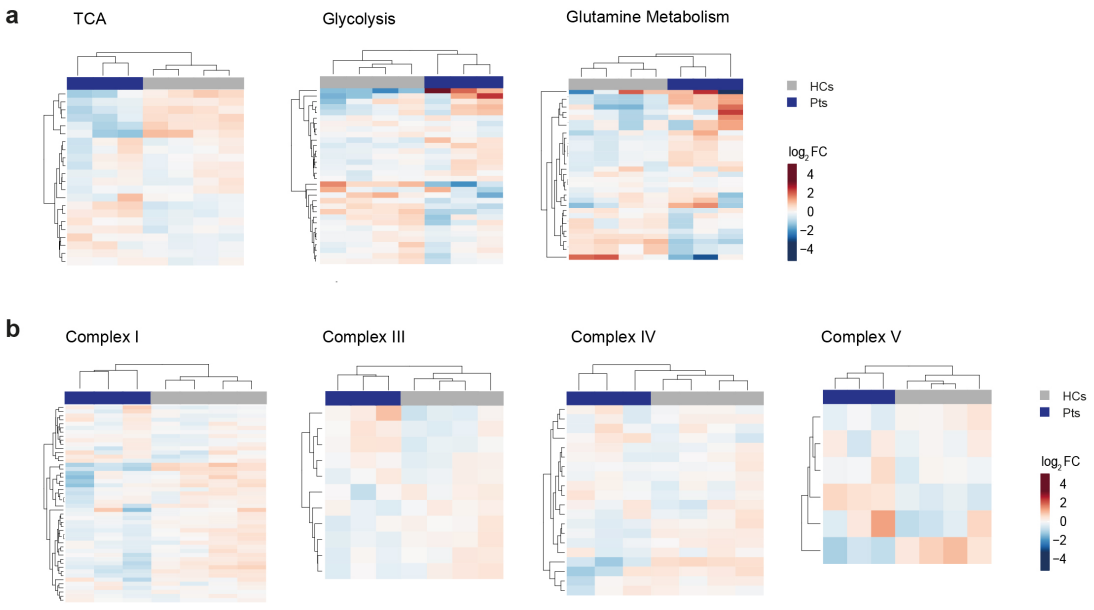
a
TCA
Glycolysis
Glutamine Metabolism
HCs
Pts
log2 FC
4
2
0
−2
−4
b
Complex I
Complex III
Complex IV
Complex V
HCs
Pts
log2 FC
4
2
0
−2
−4

**Supplementary Figure 3**

**PPBL B cells have an inflammatory transcriptional profile**

(**a**) Heatmap visualization of relative transcript abundance of genes involved in TCA, glycolysis and glutamine metabolism, in primary MZ-like B cells from HCs (n = 4) and primary B cells form PPBL patients (n = 3). (**b**) Heatmap visualization or relative transcript abundance of genes involved in respiratory complexes I, III, IV and V in primary MZ-like B cells from HCs (n = 4) and primary B cells form PPBL patients (n = 3).

## Figure S4

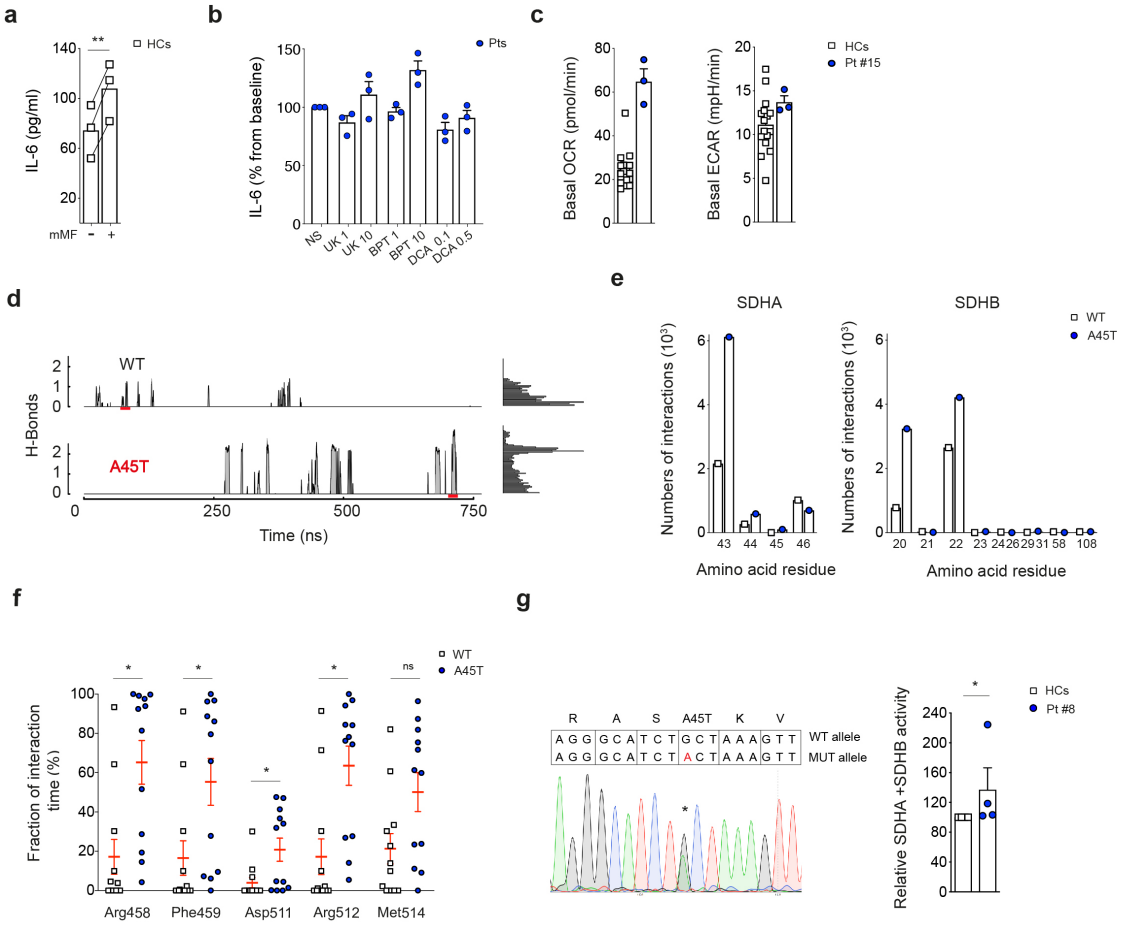
a
b
c
d
e
f
g
IL-6 (pg/ml)
HCs
mMF
IL-6 (% from baseline)
Pts
NS
UK 1
UK 10
BPT 1
BPT 10
DCA 0.1
DCA 0.5
Basal OCR (pmol/min)
Basal ECAR (mpH/min)
Pt #15
H-Bonds
WT
A45T
Time (ns)
SDHA
SDHB
Numbers of interactions (10³)
Amino acid residue
Fraction of interaction time (%)
Arg458
Phe459
Asp511
Arg512
Met514
R A S A45T K V
WT allele
MUT allele
Relative SDHA +SDHB activity
Pt #8

**Supplementary Figure 4**

## SDH drives an inflammatory phenotype in PPBL B cells

(**a**) Production of IL-6 by MZ-like B-LCLs from HCs (n = 3), quantified in cell culture supernatants of cells activated for 48 hours with IL-21 plus CD40L, in presence or absence of monomethyl fumarate. (**b**) Production of IL-6 by Patients B-LCLs (n = 3), quantified in cell culture supernatants of cells cultured for 24 hours in presence or absence of UK-5099 (1, 10 µM), BPTES (1, 10 µM) or dichloroacetate (DCA; 0.1, 0.5 mM). (**c**) OCR and ECAR measurements of primary B cells from healthy controls (n=16) and primary B cells from Patient #15 (PPBL patient). Basal values are shown. (**d**) Number of hydrogen bonds formed over time between SDHB and residues 43-46 of SDHA, wild type (wt vs. A45T). Red segments highlight the trajectory extract shown in **Video V1**. Corresponding frequency distributions of the counted hydrogen bonds are shown in the insets. Experiment was repeated independently 12 times with similar results (**e**) Frequency distributions of the residues from the N-terminal SDHA (left) and SDHB (right) involved in inter-domain hydrogen bonds in simulations with SDHA wt and SDHA A45T. (**f**) Time fraction of simulated contacts between Ala/Thr45 and adjacent SDHA residues (Arg458, Phe459, Asp511, Arg512 and Met514), depicted as a percentage of the SDHA-SDHB interaction time in wt and A45T. Experiment was repeated independently 12 times with similar results. (**g**) Visualization of Sanger sequencing of B-LCL derived cDNA of Patient 8, carrying the A45T mutation (left). Asterisk indicates changes of nucleotide G to A at position 133. Compound SDHA plus SDHB activity (enzyme complex derived from B-LCLs) from Patient 8 relative to HCs (n = 3) (right). Compound SDHA-SDHB activity was independently tested 4 times in Patient 8 and in the control subject.

Pooled data are represented as mean ± SEM. Statistical significance assessed by two-sided paired t-test (**a**), two-sided unpaired t-test (**g**), one-way ANOVA, adjustments were made for multiple comparisons with BH procedure (**f**). * $p < 0.05$, ** $p < 0.01$, ns, not significant.

## Figure S5

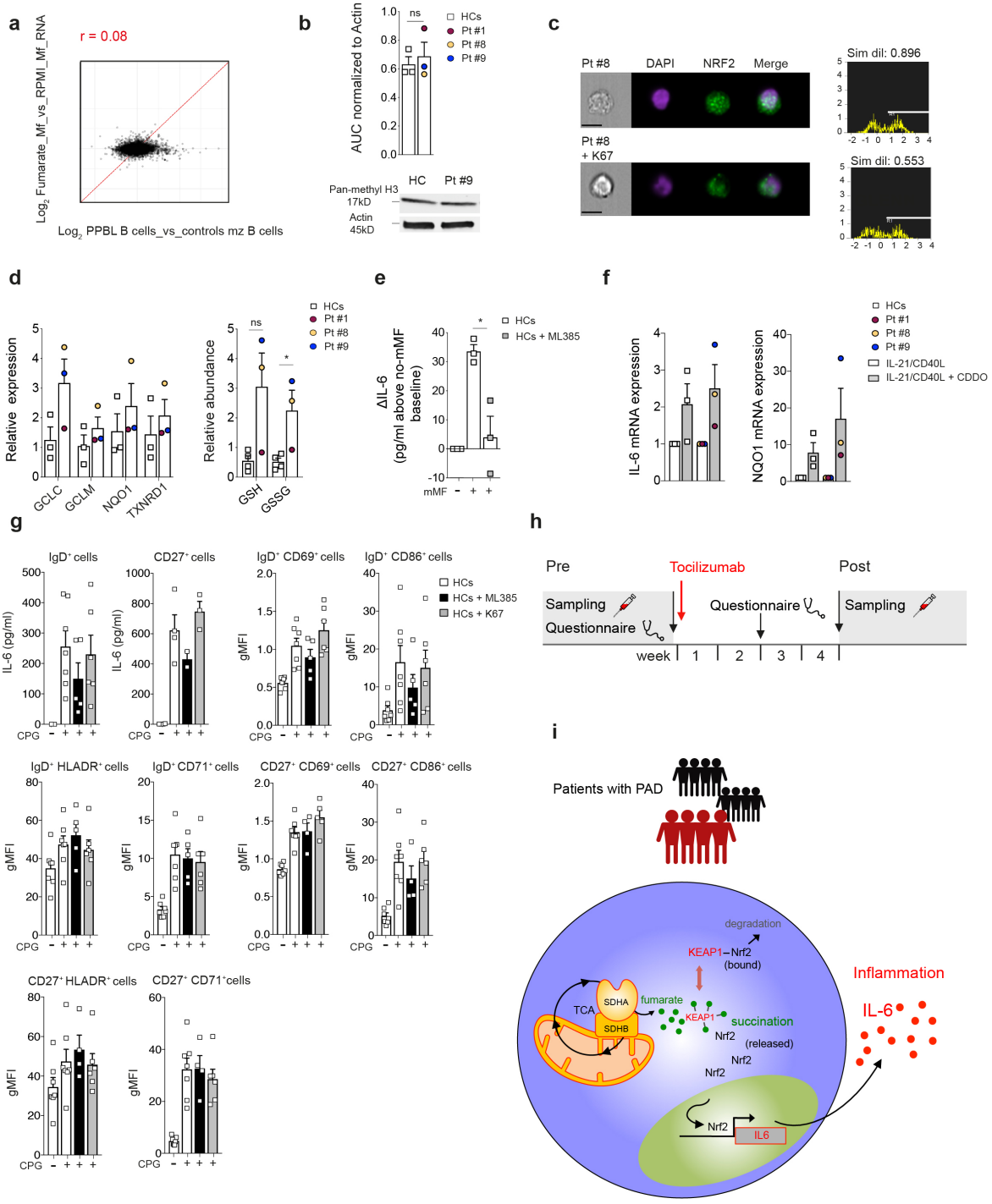
a
r = 0.08
Log2 Fumarate_Mf_vs_RPMI_Mf_RNA
Log2 PPBL B cells_vs_controls mz B cells
b
AUC normalized to Actin
ns
HCs
Pt #1
Pt #8
Pt #9
HC
Pt #9
Pan-methyl H3
17kD
Actin
45kD
c
Pt #8
DAPI
NRF2
Merge
Pt #8
+ K67
Sim dil: 0.896
Sim dil: 0.553
d
Relative expression
GCLC
GCLM
NQO1
TXNRD1
Relative abundance
GSH
GSSG
ns
*
HCs
Pt #1
Pt #8
Pt #9
e
ΔIL-6
(pg/ml above no-mMF
baseline)
*
HCs
HCs + ML385
mMF
f
IL-6 mRNA expression
NQO1 mRNA expression
HCs
Pt #1
Pt #8
Pt #9
IL-21/CD40L
IL-21/CD40L + CDDO
g
IgD+ cells
CD27+ cells
IgD+ CD69+ cells
IgD+ CD86+ cells
IL-6 (pg/ml)
gMFI
CPG
HCs
HCs + ML385
HCs + K67
IgD+ HLADR+ cells
IgD+ CD71+ cells
CD27+ CD69+ cells
CD27+ CD86+ cells
CD27+ HLADR+ cells
CD27+ CD71+ cells
h
Pre
Tocilizumab
Post
Sampling
Questionnaire
Questionnaire
Sampling
week
1
2
3
4
i
Patients with PAD
degradation
KEAP1–Nrf2
(bound)
TCA
SDHA
SDHB
fumarate
KEAP1
succination
Nrf2
(released)
Nrf2
Nrf2
Nrf2
IL6
Inflammation
IL-6

**Supplementary Figure 5**

## Fumarate drives Nrf2-dependent transcription of IL-6

(**a**) Comparison of genes that were differentially expressed between non-treated and fumarate-treated monocytes (y-axis) and those differentially expressed between primary MZ-like B cells from HCs (n = 4) and primary B cells from PPBL patients (n = 3) (x-axis). (**b**) Representative immunoblot probing for histone H3 methylation among primary B cells of a HC vs. PPBL patient. The bar graph summarizes data from HCs (n = 3) and PPBL patients (n = 3). (**c**) Representative imaging flow cytometry data showing nuclear abundance of Nrf2 in primary PPBL B cells in presence/absence of the Nrf2 inhibitor, K67. Black scale bar, 7 μm. Histograms depict similarity dilate scores of NRF2 nuclear localization in presence of absence of K67. Experiment was performed once. (**d**) mRNA abundance of canonical NRF2 regulated genes in PPBL B cell lines (n = 3) and cell lines derived from marginal zone-like B cells from HCs (n=3) (left). Abundance of GSH and GSSG from primary B cells (right) (**e**) Quantification of IL-6 production by MZ-like B-LCLs from HCs (n = 3) of cells incubated with monomethyl fumarate for 48 hours in presence vs. absence of the Nrf2 inhibitor, ML385. (**f**) mRNA abundance of NQO1 and IL6 from PPBL (n=3) and healthy MZ (n=3) B-LCLs activated with IL-21 plus CD40L in the presence or absence of the NRF2 activator, CDDO (1 μM). (**g**) Effect of Nrf2 inhibition using K67 on IL-6 production, and expression of activation markers, in primary naïve and memory B cells from healthy donors activated with CpG (2.5 μg/ml) for 24 hours (n = 5 healthy donors). (**h**) Schematic summary of the clinical trial performed in Patient 8. (**i**) Graphical summary of the model proposed from this study.
Pooled data are shown as mean ± SEM. Correlation in (**a**) was assessed using Pearson's r, statistical significance was assessed by two-sided unpaired t-test (**b**,**e**,**d** [right]), two way ANOVA (**d** [left]).

# Figure 1

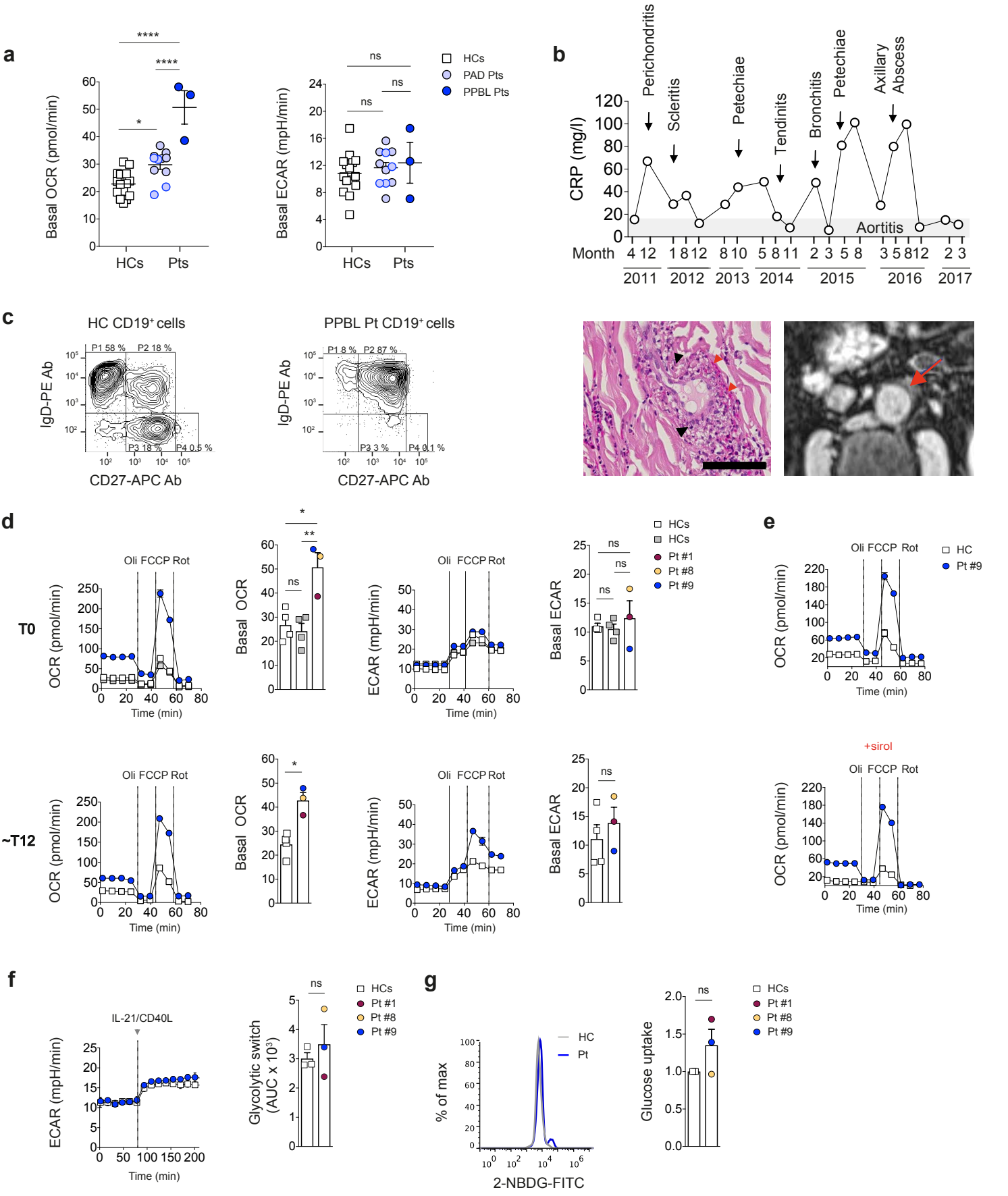
a
Basal OCR (pmol/min)
HCs
Pts
Basal ECAR (mpH/min)
HCs
PAD Pts
PPBL Pts
b
CRP (mg/l)
Perichondritis
Scleritis
Petechiae
Tendinits
Bronchitis
Petechiae
Axillary Abscess
Aortitis
Month
2011
2012
2013
2014
2015
2016
2017
c
HC CD19+ cells
PPBL Pt CD19+ cells
IgD-PE Ab
CD27-APC Ab
d
T0
~T12
Oli FCCP Rot
OCR (pmol/min)
Time (min)
Basal OCR
ECAR (mpH/min)
Basal ECAR
HCs
Pt #1
Pt #8
Pt #9
e
HC
Pt #9
+sirol
f
IL-21/CD40L
Glycolytic switch (AUC x 10³)
g
% of max
2-NBDG-FITC
Glucose uptake

# Figure 2

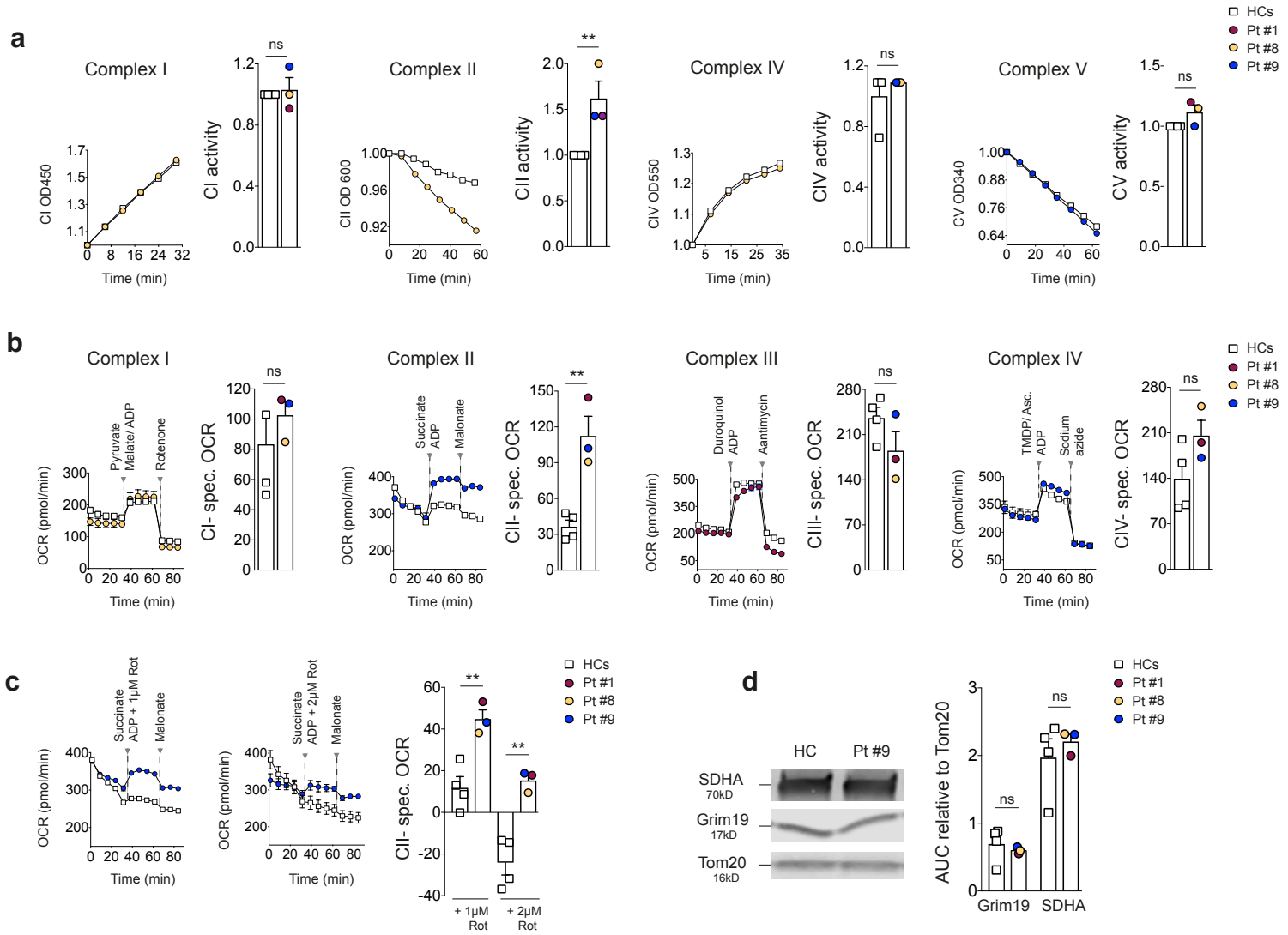
a
Complex I
CI OD450
Time (min)
CI activity
ns
Complex II
CII OD 600
Time (min)
CII activity
**
Complex IV
CIV OD550
Time (min)
CIV activity
ns
Complex V
CV OD340
Time (min)
CV activity
ns
HCs
Pt #1
Pt #8
Pt #9
b
Complex I
Pyruvate
Malate/ ADP
Rotenone
OCR (pmol/min)
Time (min)
CI- spec. OCR
ns
Complex II
Succinate
ADP
Malonate
CII- spec. OCR
**
Complex III
Duroquinol
ADP
Aantimycin
CIII- spec. OCR
ns
Complex IV
TMDP/ Asc.
ADP
Sodium
azide
CIV- spec. OCR
ns
c
Succinate
ADP + 1µM Rot
Malonate
Succinate
ADP + 2µM Rot
Malonate
CII- spec. OCR
**
**
+ 1µM
Rot
+ 2µM
Rot
d
HC
Pt #9
SDHA
70kD
Grim19
17kD
Tom20
16kD
AUC relative to Tom20
ns
ns
Grim19
SDHA

# Figure 3

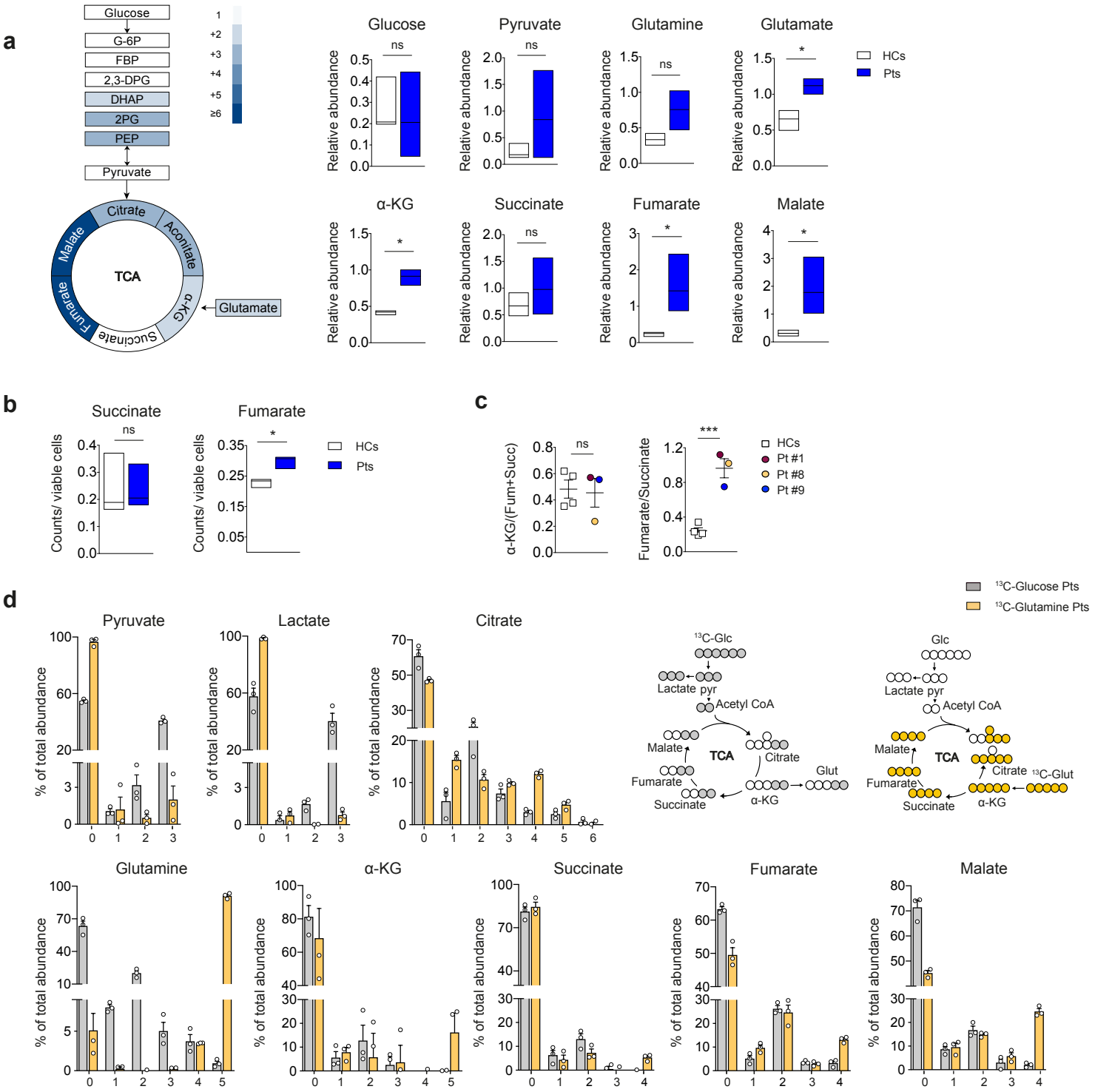
a
Glucose
G-6P
FBP
2,3-DPG
DHAP
2PG
PEP
Pyruvate
1
+2
+3
+4
+5
≥6
Citrate
Aconitate
α-KG
Succinate
Fumarate
Malate
TCA
Glutamate
Glucose
Pyruvate
Glutamine
Glutamate
α-KG
Succinate
Fumarate
Malate
Relative abundance
ns
*
HCs
Pts
b
Succinate
Fumarate
Counts/ viable cells
ns
*
HCs
Pts
c
α-KG/(Fum+Succ)
Fumarate/Succinate
ns
***
HCs
Pt #1
Pt #8
Pt #9
d
13C-Glucose Pts
13C-Glutamine Pts
Pyruvate
Lactate
Citrate
Glutamine
α-KG
Succinate
Fumarate
Malate
% of total abundance
13C-Glc
Lactate pyr
Acetyl CoA
TCA
Malate
Citrate
Fumarate
Succinate
α-KG
Glut
Glc
13C-Glut

# Figure 4

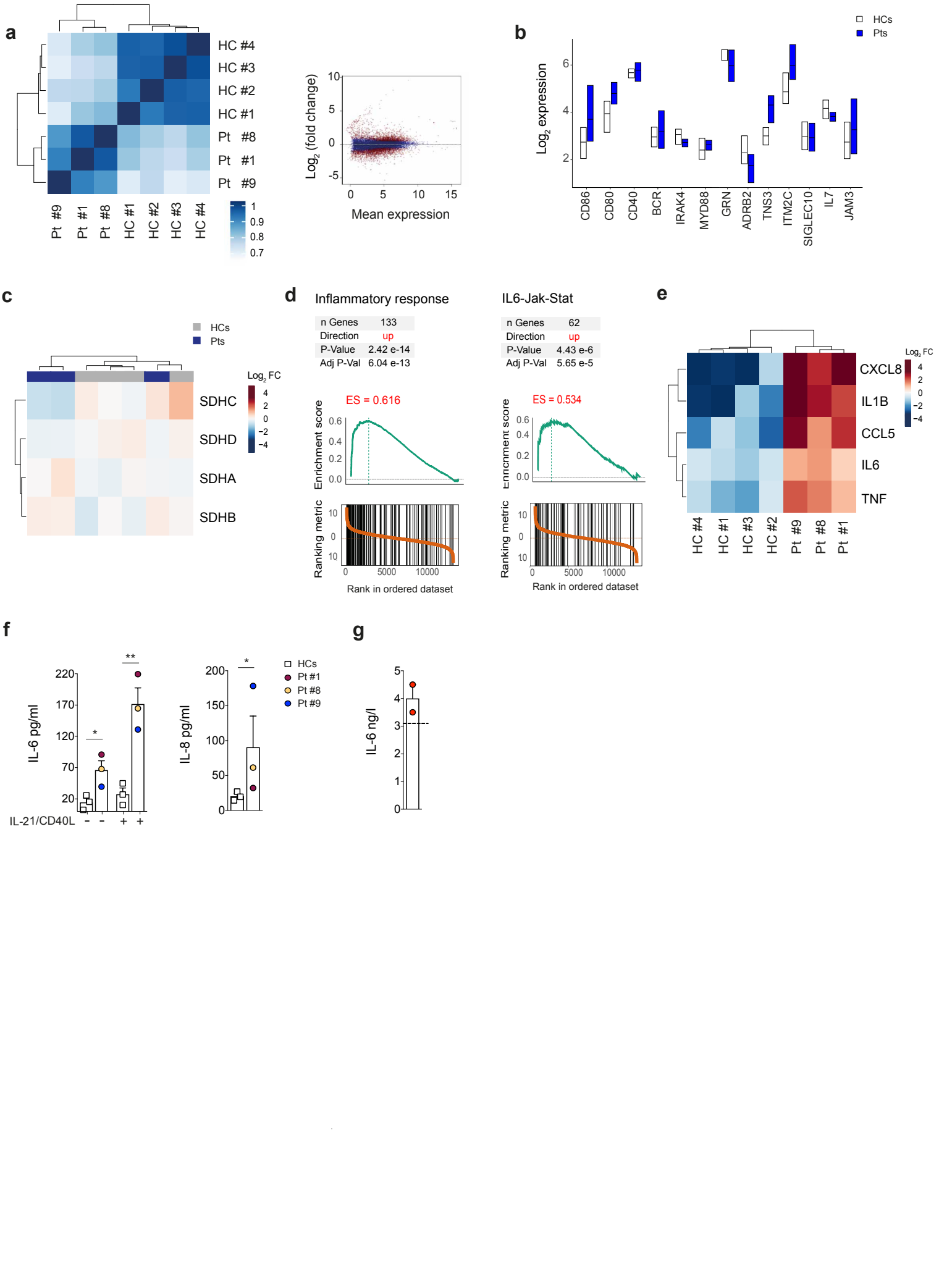
a
HC #4
HC #3
HC #2
HC #1
Pt #8
Pt #1
Pt #9
Pt #9
Pt #1
Pt #8
HC #1
HC #2
HC #3
HC #4
1
0.9
0.8
0.7
Log2 (fold change)
Mean expression
b
HCs
Pts
Log2 expression
CD86
CD80
CD40
BCR
IRAK4
MYD88
GRN
ADRB2
TNS3
ITM2C
SIGLEC10
IL7
JAM3
c
HCs
Pts
Log2 FC
SDHC
SDHD
SDHA
SDHB
d
Inflammatory response
n Genes 133
Direction up
P-Value 2.42 e-14
Adj P-Val 6.04 e-13
ES = 0.616
Enrichment score
Ranking metric
Rank in ordered dataset
IL6-Jak-Stat
n Genes 62
Direction up
P-Value 4.43 e-6
Adj P-Val 5.65 e-5
ES = 0.534
Enrichment score
Ranking metric
Rank in ordered dataset
e
Log2 FC
CXCL8
IL1B
CCL5
IL6
TNF
HC #4
HC #1
HC #3
HC #2
Pt #9
Pt #8
Pt #1
f
IL-6 pg/ml
IL-8 pg/ml
IL-21/CD40L
HCs
Pt #1
Pt #8
Pt #9
g
IL-6 ng/l

# Figure 5

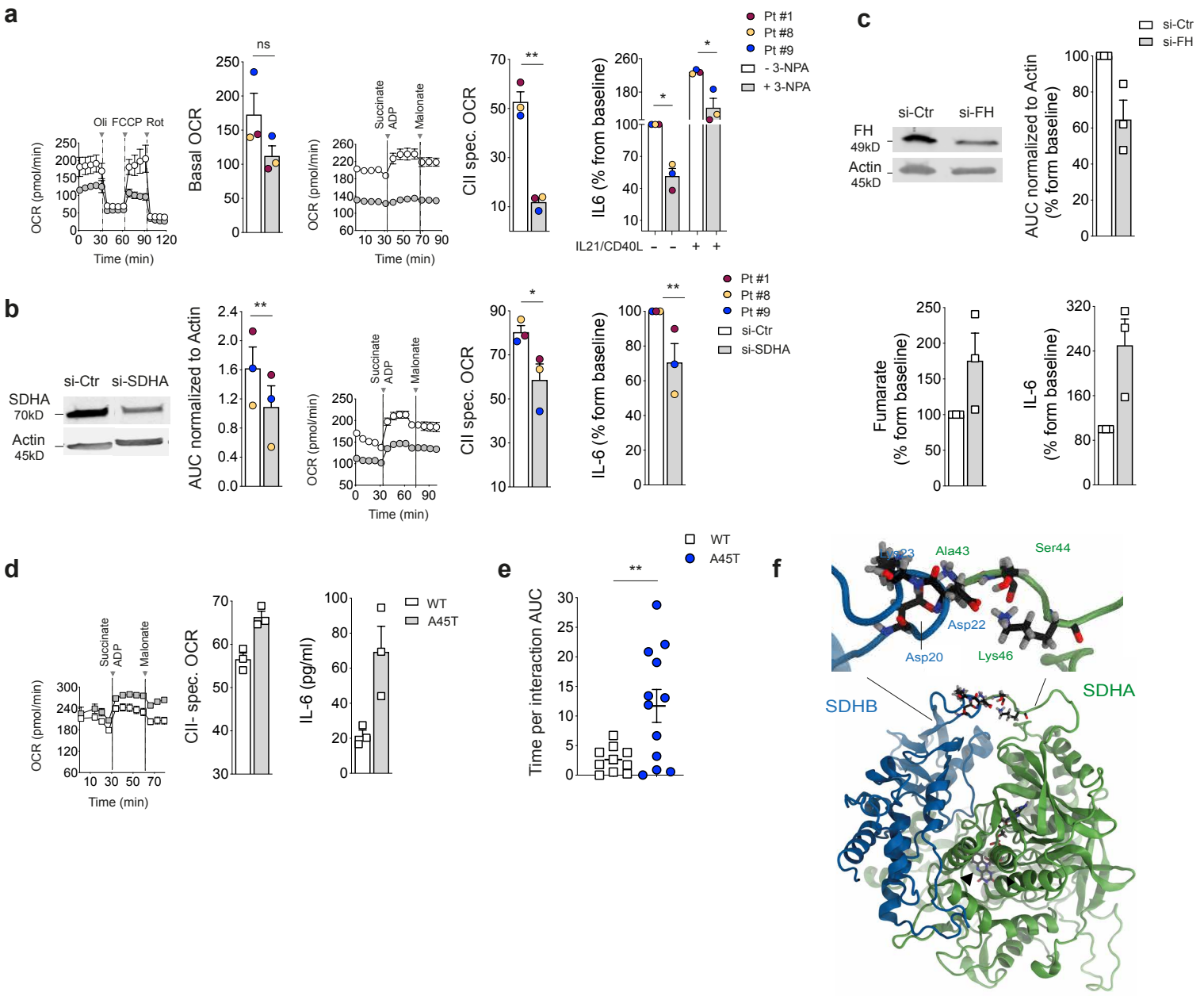
a
Oli FCCP Rot
OCR (pmol/min)
Time (min)
Basal OCR
ns
Succinate
ADP
Malonate
CII spec. OCR
**
IL6 (% from baseline)
*
Pt #1
Pt #8
Pt #9
- 3-NPA
+ 3-NPA
IL21/CD40L
b
si-Ctr
si-SDHA
SDHA
70kD
Actin
45kD
AUC normalized to Actin
IL-6 (% form baseline)
Pt #1
Pt #8
Pt #9
si-Ctr
si-SDHA
c
si-Ctr
si-FH
FH
49kD
Actin
45kD
AUC normalized to Actin
(% form baseline)
Fumarate
(% form baseline)
IL-6
(% form baseline)
d
Succinate
ADP
Malonate
OCR (pmol/min)
Time (min)
CII- spec. OCR
IL-6 (pg/ml)
WT
A45T
e
**
WT
A45T
Time per interaction AUC
f
Ala43
Ser44
Asp22
Asp20
Lys46
SDHB
SDHA

# Figure 6

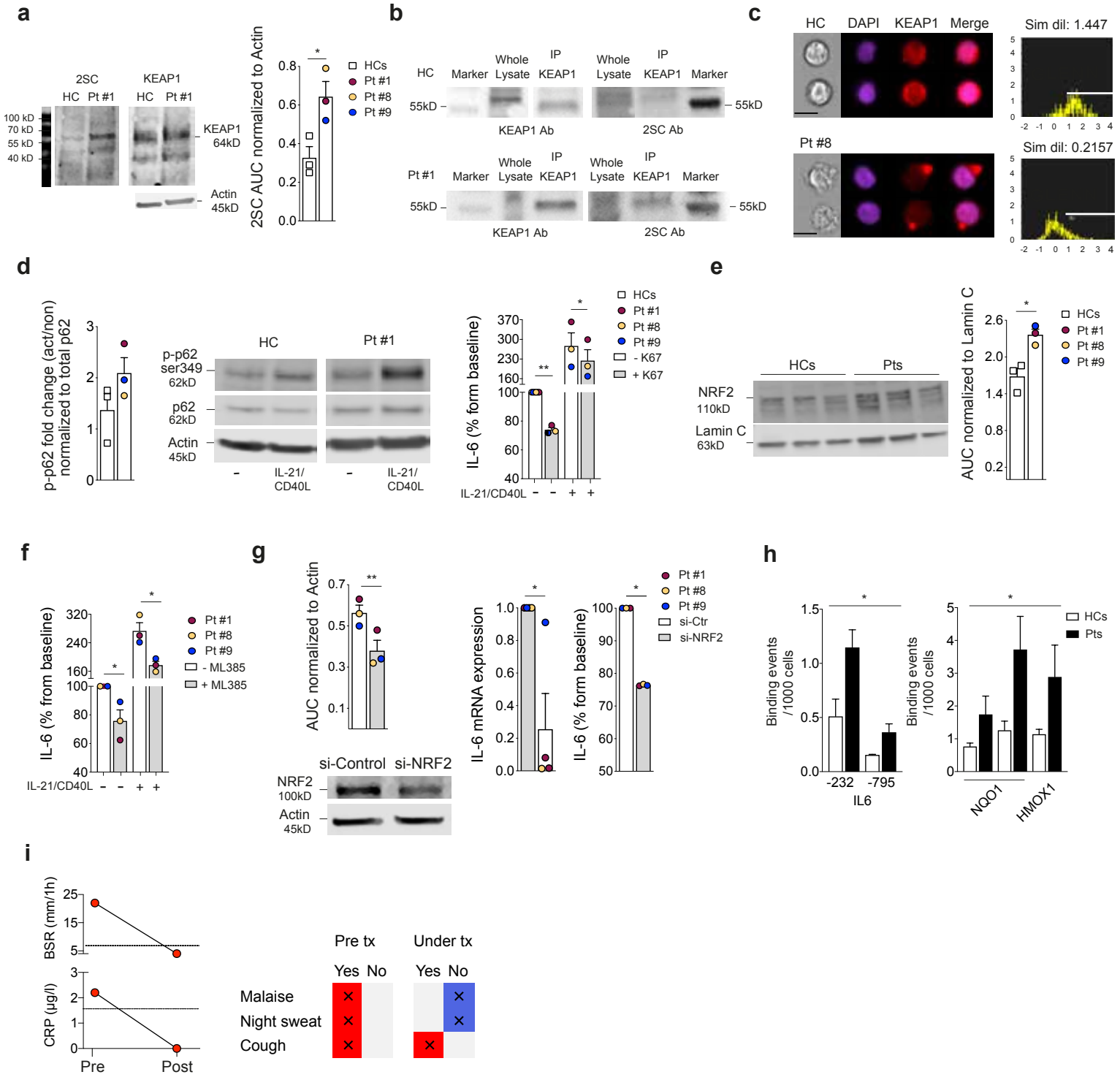
a
2SC
KEAP1
HC Pt #1
HC Pt #1
100 kD
70 kD
55 kD
40 kD
KEAP1 64kD
Actin 45kD
2SC AUC normalized to Actin
HCs
Pt #1
Pt #8
Pt #9
b
HC
Marker
Whole Lysate
IP KEAP1
55kD
KEAP1 Ab
2SC Ab
Pt #1
c
HC
DAPI
KEAP1
Merge
Pt #8
Sim dil: 1.447
Sim dil: 0.2157
d
p-p62 fold change (act/non) normalized to total p62
p-p62 ser349 62kD
p62 62kD
Actin 45kD
IL-21/ CD40L
IL-6 (% form baseline)
IL-21/CD40L
- K67
+ K67
e
HCs
Pts
NRF2 110kD
Lamin C 63kD
AUC normalized to Lamin C
f
IL-6 (% from baseline)
- ML385
+ ML385
g
AUC normalized to Actin
si-Control
si-NRF2
NRF2 100kD
Actin 45kD
IL-6 mRNA expression
IL-6 (% form baseline)
si-Ctr
si-NRF2
h
Binding events /1000 cells
IL6
-232
-795
NQO1
HMOX1
i
BSR (mm/1h)
CRP (µg/l)
Pre
Post
Pre tx
Under tx
Yes No
Malaise
Night sweat
Cough

# Figure S1

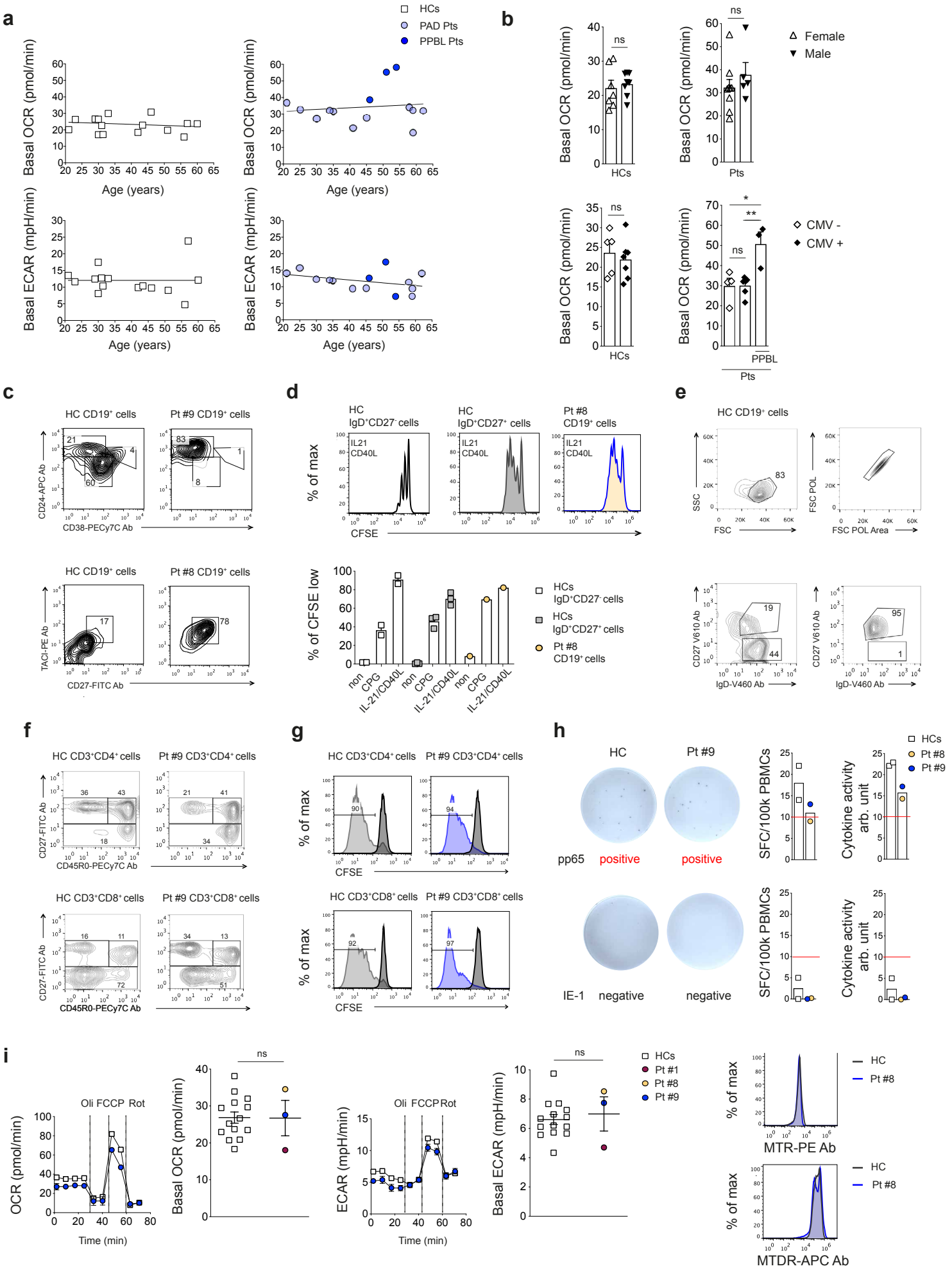
a
HCs
PAD Pts
PPBL Pts
Basal OCR (pmol/min)
Basal ECAR (mpH/min)
Age (years)
b
Basal OCR (pmol/min)
ns
HCs
Pts
Female
Male
CMV -
CMV +
PPBL
*
**
c
HC CD19+ cells
Pt #9 CD19+ cells
Pt #8 CD19+ cells
CD24-APC Ab
CD38-PECy7C Ab
TACI-PE Ab
CD27-FITC Ab
d
HC IgD+CD27- cells
HC IgD+CD27+ cells
IL21
CD40L
% of max
CFSE
% of CFSE low
non
CPG
IL-21/CD40L
HCs IgD+CD27- cells
HCs IgD+CD27+ cells
Pt #8 CD19+ cells
e
SSC
FSC
FSC POL
FSC POL Area
CD27 V610 Ab
IgD-V460 Ab
f
HC CD3+CD4+ cells
Pt #9 CD3+CD4+ cells
HC CD3+CD8+ cells
Pt #9 CD3+CD8+ cells
CD27-FITC Ab
CD45R0-PECy7C Ab
g
% of max
CFSE
h
HC
Pt #9
pp65
positive
IE-1
negative
SFC/100k PBMCs
Cytokine activity arb. unit
HCs
Pt #8
Pt #9
i
OCR (pmol/min)
Oli FCCP Rot
Time (min)
Basal OCR (pmol/min)
ECAR (mpH/min)
Basal ECAR (mpH/min)
HCs
Pt #1
Pt #8
Pt #9
% of max
MTR-PE Ab
MTDR-APC Ab
HC
Pt #8

# Figure S2

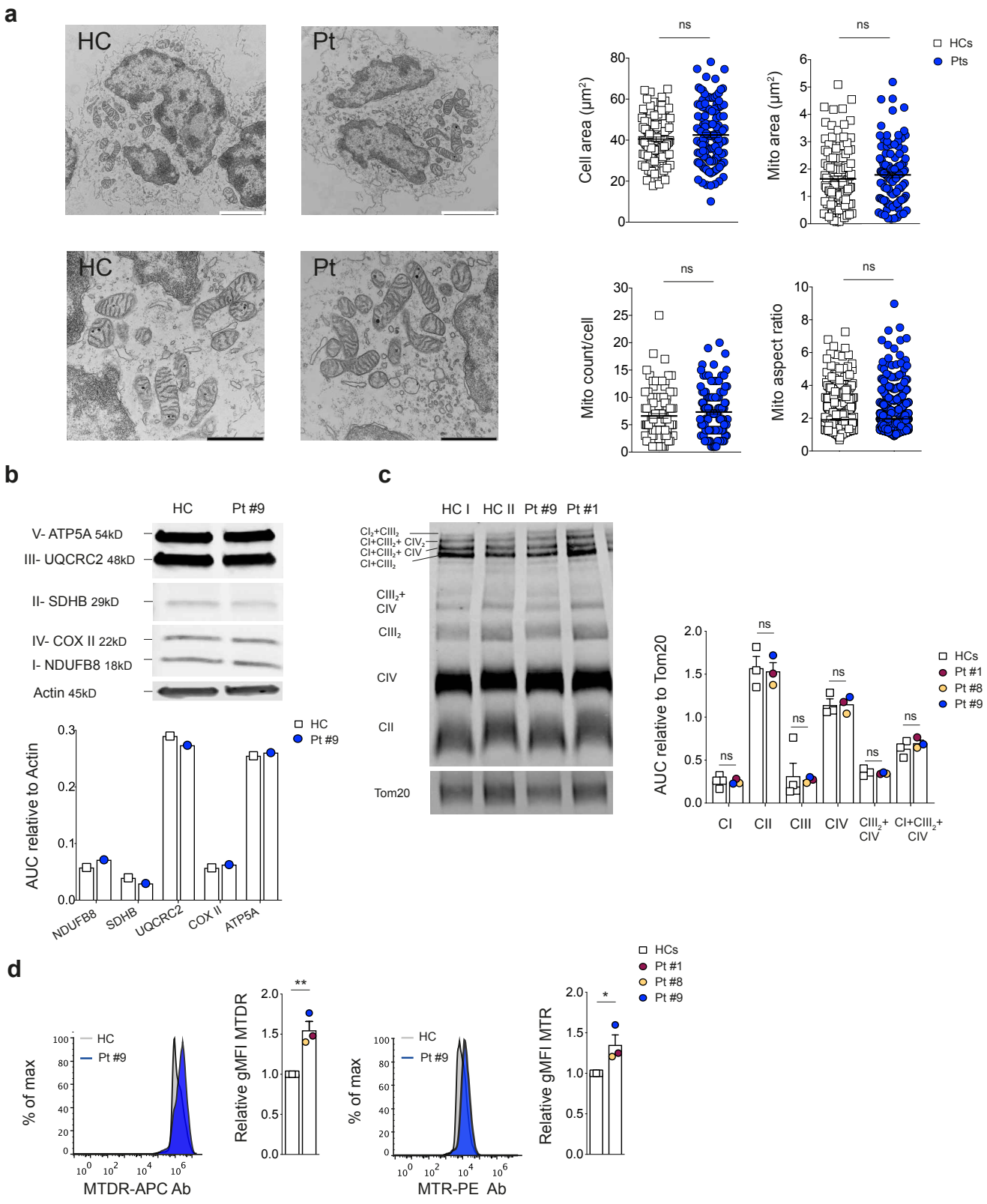
a
HC
Pt
HC
Pt
ns
Cell area (µm²)
ns
Mito area (µm²)
HCs
Pts
ns
Mito count/cell
ns
Mito aspect ratio
b
HC
Pt #9
V- ATP5A 54kD
III- UQCRC2 48kD
II- SDHB 29kD
IV- COX II 22kD
I- NDUFB8 18kD
Actin 45kD
AUC relative to Actin
HC
Pt #9
NDUFB8
SDHB
UQCRC2
COX II
ATP5A
c
HC I
HC II
Pt #9
Pt #1
CI2+CIII2
CI+CIII2+ CIV2
CI+CIII2+ CIV
CI+CIII2
CIII2+ CIV
CIII2
CIV
CII
Tom20
AUC relative to Tom20
HCs
Pt #1
Pt #8
Pt #9
CI
CII
CIII
CIV
CIII2+ CIV
CI+CIII2+ CIV
d
HC
Pt #9
% of max
MTDR-APC Ab
Relative gMFI MTDR
HC
Pt #9
% of max
MTR-PE Ab
Relative gMFI MTR
HCs
Pt #1
Pt #8
Pt #9

# Figure S3

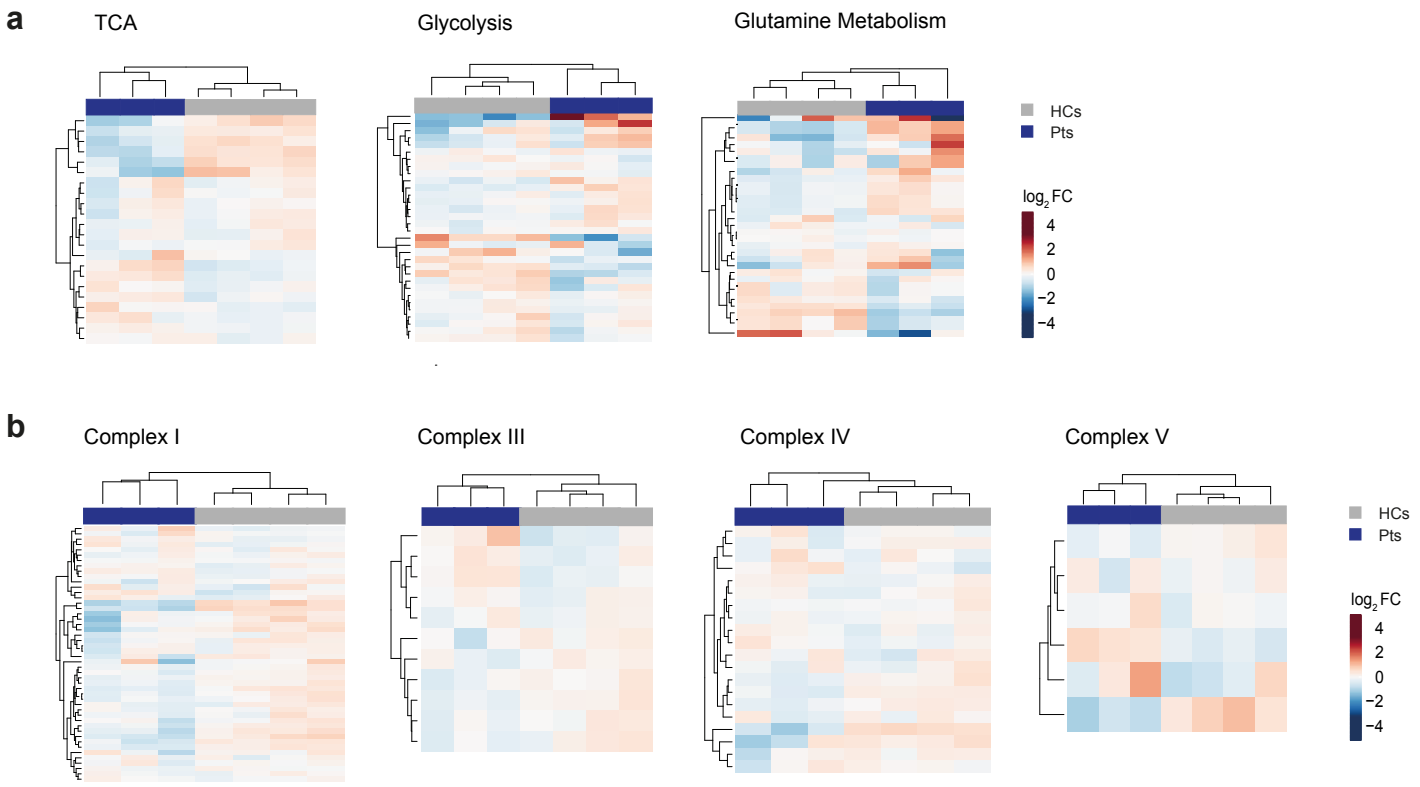
a
TCA
Glycolysis
Glutamine Metabolism
HCs
Pts
log2 FC
4
2
0
−2
−4
b
Complex I
Complex III
Complex IV
Complex V
HCs
Pts
log2 FC
4
2
0
−2
−4

# Figure S4

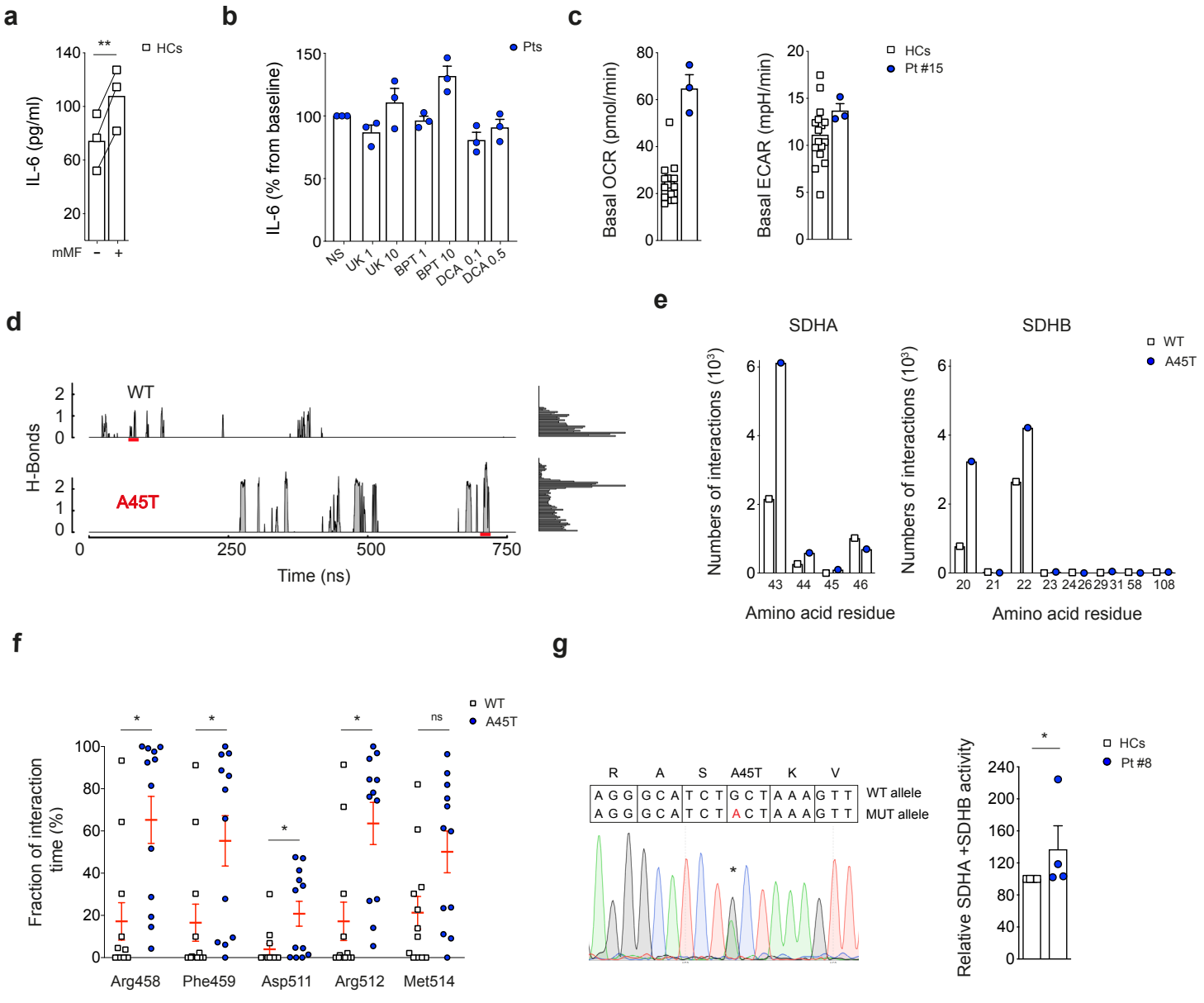
a
IL-6 (pg/ml)
HCs
mMF
b
IL-6 (% from baseline)
Pts
NS
UK 1
UK 10
BPT 1
BPT 10
DCA 0.1
DCA 0.5
c
Basal OCR (pmol/min)
Basal ECAR (mpH/min)
HCs
Pt #15
d
H-Bonds
WT
A45T
Time (ns)
e
SDHA
SDHB
WT
A45T
Numbers of interactions (10³)
Amino acid residue
f
Fraction of interaction time (%)
WT
A45T
Arg458
Phe459
Asp511
Arg512
Met514
g
R A S A45T K V
WT allele
MUT allele
Relative SDHA +SDHB activity
HCs
Pt #8

# Figure S5

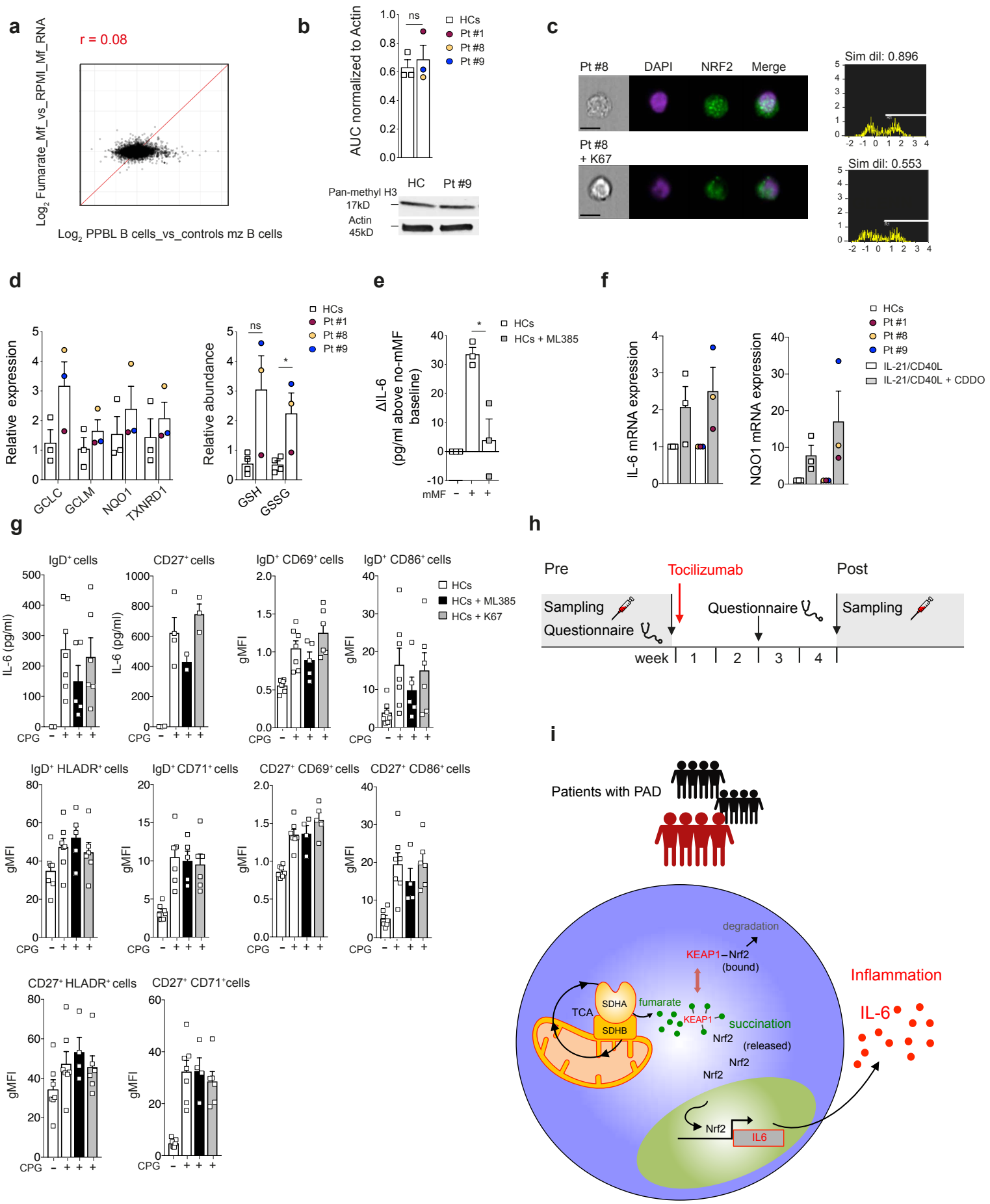
a
r = 0.08
Log2 Fumarate_Mf_vs_RPMI_Mf_RNA
Log2 PPBL B cells_vs_controls mz B cells
b
AUC normalized to Actin
ns
HCs
Pt #1
Pt #8
Pt #9
HC
Pt #9
Pan-methyl H3
17kD
Actin
45kD
c
Pt #8
DAPI
NRF2
Merge
Pt #8
+ K67
Sim dil: 0.896
Sim dil: 0.553
d
Relative expression
GCLC
GCLM
NQO1
TXNRD1
Relative abundance
GSH
GSSG
e
ΔIL-6
(pg/ml above no-mMF
baseline)
HCs
HCs + ML385
mMF
f
IL-6 mRNA expression
NQO1 mRNA expression
IL-21/CD40L
IL-21/CD40L + CDDO
g
IgD+ cells
CD27+ cells
IgD+ CD69+ cells
IgD+ CD86+ cells
IL-6 (pg/ml)
gMFI
HCs
HCs + ML385
HCs + K67
CPG
IgD+ HLADR+ cells
IgD+ CD71+ cells
CD27+ CD69+ cells
CD27+ CD86+ cells
CD27+ HLADR+ cells
CD27+ CD71+cells
h
Pre
Tocilizumab
Post
Sampling
Questionnaire
Questionnaire
Sampling
week
1
2
3
4
i
Patients with PAD
degradation
KEAP1–Nrf2
(bound)
TCA
SDHA
SDHB
fumarate
KEAP1
succination
Nrf2
(released)
Nrf2
Nrf2
Nrf2
IL6
Inflammation
IL-6

**Table S1**
**a**

| Pt | Sex | Age (at dx) | Infection | Lymphoproliferation | Autoimmunity | Others |
|---|---|---|---|---|---|---|
| ♯1 | f | 46 | herpes simplex, sinusitis, bronchitis | hepatomegaly | raynaud syndrome | athralgia, spontanious, rib fractures |
| ♯2 | f | 45 | bronchitis, pneumonia | splenomegaly | | athralgia |
| ♯3 | m | 21 | sinusitis, bronchitis pneumonia | splenomegaly, retroperitoneal lymphadenopathy | vitiligo | |
| ♯4 | f | 62 | postinterventional wound infections | | | |
| ♯5 | m | 58 | | splenomegaly, axilar lymphadenopathy | autoimmune thrombocytopenia | |
| ♯6 | m | 30 | | splenomegaly | autoimmune hemolytic anaemia/ thrombocytopenia | aphthous ulcers |
| ♯7 | m | 25 | akne inversa, skin abscesses | mild splenomegaly | | |
| ♯8 | f | 51 | otitis, sinusitis, bronchitis, candida oesophagitis | mild splenomegaly | | fatigue, weight loss |
| ♯9 | m | 54 | bronchitis | mild splenomegaly | perichondritis, scleritis, tendinis, vascultis | |
| ♯10 | f | 41 | bronchitis, sinusitis, pneumonia | bilateral hilar lymphadenopathy | | fatigue |
| ♯11 | f | 35 | bronchits, sinusitis | | diabetes mellitus | |
| ♯12 | f | 59 | bronchits, pyelonephritis | | spondylarthritis | |
| ♯13 | f | 34 | sinusitis | | autoimmune keratitis | fatigue |
| ♯14 | f | 59 | bronchitis, pneumonia, urinary tract infections | retroperitoneal lymphadenopathy | autoimmune thrombocytopenia/ neutropenia | |
| ♯15 | f | 42 | recurrent sinusitis, meningitis in 1st year of life | | Lupus like disease (ANA, Anti-DNS), Polyarthritis, mild nephropathy | fatigue |

**b**

| | IgG g/l | IgM g/l | Naïve / µl<br>$CD19^+$ $CD27^-$ $IgD^+$ $IgM^+$ | Marginal zone like / µl<br>$CD19^+$ $CD27^+$ $IgD^+$ $IgM^+$ | Class switched /µl<br>$CD19^+$ CD27+ $IgD^-$ $IgM^-$ | CD21low /µl<br>$CD19^+$ $CD21^{low}$ $CD38^-$ | Transitional /µl<br>$CD19^+$ $CD38^+$ $IgD^+$ $IgM^+$ | Plasmablasts /µl<br>$CD19^+$ $CD38^{++}$ $IgD^-$ $IgM^-$ |
|---|---|---|---|---|---|---|---|---|
| Ref value | 1-7 | 0.4-2.3 | 66-228 | 8-172 | 8-102 | 1-12 | 1-5 | 1-5 |
| Pt | | | | | | | | |
| ♯1 | 5.9 | 9.04 | 225 | 2471 | 82 | 94 | 6 | <3 |
| ♯2 | IgG4< 0.05 | 2.76 | 128 | 72 | 28 | 5 | 6 | <1 |
| ♯3 | 0.9 | 0.22 | 143 | 28 | <1 | 6 | 2 | <1 |
| ♯4 | 5.8 | 2.19 | 87 | 33 | 16 | 4 | 4 | 1 |
| ♯5 | 3.4 | 0.45 | 150 | 99 | 4 | 8 | 6 | <1 |
| ♯6 | 4.3 | 0.22 | 95 | 13 | 2 | 5 | <1 | <1 |
| ♯7 | 6.7 | 0.36 | 244 | 33 | 9.1 | 3 | 5 | <1 |
| ♯8 | 4.4 | 4.47 | 554 | 2168 | 11 | 39 | 3 | <3 |
| ♯9 | 5 | 7.75 | 276 | 455 | 28 | 71 | 9 | 5 |
| ♯10 | 2.85 | 0.24 | 332 | 32 | 5 | 6 | 11 | <1 |
| ♯11 | 3.5 | 1.15 | 81 | 86 | 11 | 1 | 1 | <1 |
| ♯12 | 3.6 | | 289 | 74 | 16 | 3 | 10 | <1 |
| ♯13 | 6.3 | 2.21 | 156 | 92 | 69 | 2 | 5 | <1 |
| ♯14 | 1.6 | 1.47 | 170 | 3 | <1 | 40 | 9 | <1 |
| ♯15 | 6.1 | 10 | 1006 | 367 | 125 | 112 | 17 | <1 |

**c**

| | CD4 Naïve relative | CD4 Central memory | CD4 Effector memory | CD4 TEMRA | CD4 Follicular T helper | CD4 Recent thymic emigrants (RTE) | CD4 Treg | CD4 activated |
|---|---|---|---|---|---|---|---|---|
| Ref value | 15.7-54.7 % of $CD4^+$ T cells | 8-28.8% of $CD4^+$ T cells | 16.8-57.4% of $CD4^+$ T cells | 3.6-23.2% of $CD4^+$ T cells | 6.9-19.1% of $CD4^+$ T cells | 14.1-37.2% of naïve $CD4^+$ T cells | 6.1-11% of $CD4^+$ T cells | 4.5-15.6% of $CD4^+$ T cells |
| Pt | | | | | | | | |
| ♯1 | 33.80 | 26.50 | 33.30 | 6.40 | 18.50 | 21.90 | 11.70 | 5.60 |
| ♯8 | 49.50 | 24.30 | 22.00 | 4.10 | 9.90 | 20.90 | 6.60 | 3.90 |
| ♯9 | 18.70 | 34.50 | 43.60 | 3.10 | 19.00 | 9.00 | 11.20 | 8.80 |
| ♯15 | 13.00 | 37.50 | 47.10 | 2.40 | 25.40 | 7.00 | 4.90 | 4.80 |

| | CD8 naïve relative | CD8 Central memory | CD8 Effector memory | CD8 TEMRA | CD8 activated |
|---|---|---|---|---|---|
| Ref value | 7-62.5% of $CD8^+$ T cells | 0.6-4.4% of $CD8^+$ T cells | 4.3-64.5% of $CD8^+$ T cells | 8.1-60.5% of $CD8^+$ T cells | 5.7-48.2% of $CD8^+$ T cells |
| Pt | | | | | |
| ♯1 | 50.40 | 6.30 | 28.40 | 14.90 | 9.70 |
| ♯8 | 43.50 | 4.90 | 28.30 | 23.20 | 9.10 |
| ♯9 | 27.50 | 6.70 | 24.80 | 41.00 | 34.40 |
| ♯15 | 20.50 | 8.80 | 40.80 | 29.90 | 16.80 |

## Table S2

| Pt | Chr | Basepair | pos. cDNA | Zygosity | Gene symbol | Amino acid | rsID | ESP | CADD-PHRED | Poly Phen2 | SIFT score |
|---|---|---|---|---|---|---|---|---|---|---|---|
| ♯1 | 5 | 225975 | c.C405T | HET | SDHA | G135G | rs61733344 | 0.001 | 20.4 | NA | NA |
| ♯8 | 5 | 223551 | c.G133A | HET | SDHA | A45T | rs140736646 | 0 | 23 | 0.002 | 0.16 |
| ♯9 | 5 | 236513 | c.C1346T | HET | SDHA | A449V | rs201139276 | NA | 26.8 | 0.585 | 0.02 |
| ♯15 | 5 | 256483 | c.1945_1946delTT | HET | SDHA | L649Efs | rs112307877 | 0 | 33 | NA | NA |

Chr = chromosome; rsID = single nucleotide polymorphism database identifier; ESP = Grand Opportunity Exome Sequencing Project; CADD = Combined Annotation Dependent Depletion; PolyPhen2 = Polymorphism Phenotyping 2; SIFT = Sorting Intolerant from Tolerant; NA = Not Applicable

## Table S3

| ARE sequence | ARE orientation | Position of ARE | Gene | Entrez Gene ID | UCSC ID |
|---|---|---|---|---|---|
| ATTACTATGCG | sense | -795 | IL6 | 3569 | uc064bxs.1 |
| GTGACTCAGCA | antisense | -232 | | | uc064bxt.1 |
| GTGATGTAGCC | antisense | -2924 | IL1b | 3553 | uc002tii.2 |
| GTGATCATGCA | sense | -2129 | | | |
| TTTACATAGCA | sense | -1573 | CXCL8 | 3576 | uc003hhe.3 |
| ATGATTGTGCA | sense | -1358 | | | |

## Table S4

**a**

| | Ref value | Pre-Actemra | Post-Actemra |
|---|---|---|---|
| IgG | 7.0-16.0 g/l | 7.2 | 6.4 |
| IgG1 | 4.90-11.40g/l | 4.39 | 3.7 |
| IgG2 | 1.50-6.40g/l | 2.31 | 2.05 |
| IgG3 | 0.20-1.10g/l | 0.36 | 0.34 |
| IgG4 | 0.08-1.40g/l | 0.18 | 0.16 |
| IgA | 0.70-4.00g/l | 0.56 | 0.49 |
| IgM | 0.40-2.30g/l | 4.95 | 5.21 |

**b**

| | Ref value | Pre-Actemra | Post-Actemra |
|---|---|---|---|
| T cells relative | 55-86% (of lymphocytes) | 49 | 44 |
| T cells absolute | 742-2750/µl | 1691 | 1725 |
| B cells relative | 5-22% (of lymphocytes) | 45 | 53 |
| B cells absolute | 80-616/µl | 1533 | 1964 |

**c**

| | Ref value | Pre-Actemra | Post-Actemra |
|---|---|---|---|
| Naïve B cells relative | 25.1-92.4% of B cells | 51.1 | 49.7 |
| Naïve B cells absolute | 66-228/µl | 783 | 976 |
| Marginal zone like B cells relative | 3.1-59.7% of B cells | 44.6 | 48.2 |
| Marginal zone like B cells absolute | 8-172/µl | 684 | 947 |
| Memory B cell relative | 2.4-32.6% of B cells | 0.7 | 0.9 |
| Memory B cell absolute | 8-102/µl | 11 | 18 |
| $CD21^{lo}$ B cells relative | 0.5-4.7% of B cells | 4.4 | 3.6 |
| $CD21^{lo}$ B cells absolute | 1-12/µl | 67 | 70 |
| Transitional B cells relative | 0.3-2.9% of B cells | 0.2 | 0.2 |
| Transitional B cells absolute | 1-5/µl | 3 | 4 |
| Plasmablasts relative | 0.1-3% (of B cells) | 0.1 | 0.1 |
| Plasmablasts absolute | 1-5/µl | 2 | 2 |